Check for updates

Received: 28 July 2023 | Revised: 1 February 2024 | Accepted: 2 February 2024

DOI: 10.1111/jmg.12765

ORIGINAL ARTICLE

Journal of METAMORPHIC GEOLOGY WILEY

# Dehydration-driven deformation of eclogite: Interplay between fluid discharge and rheology

**Michał Bukała**[1,2] | **Károly Hidas**[3] | **Iwona Klonowska**[4,5] | **Christopher J. Barnes**[2] | **Kathrin Fassmer**[6] | **Jarosław Majka**[4,5]

[1]Instituto Andaluz de Ciencias de la Tierra (IACT), CSIC-UGR, Armilla, Granada, Spain

[2]Institute of Geological Sciences, Polish Academy of Sciences, Kraków, Poland

[3]Instituto Geológico y Minero de España (IGME), CSIC, Granada, Spain

[4]Faculty of Geology, Geophysics and Environmental Protection, AGH University of Krakow, Kraków, Poland

[5]Department of Earth Sciences, Uppsala University, Uppsala, Sweden

[6]Department of Geology, University of Innsbruck, Innsbruck, Austria

**Correspondence**
Michał Bukała, Instituto Andaluz de Ciencias de la Tierra (IACT), CSIC-UGR, Armilla, Granada, Spain.
Email: michal.bukala@csic.es

**Funding information**
Agencia Estatal de Investigacion of the Ministerio de Ciencia e Innovacion (Spain; MCIN/AEI/10.13039/501100011033, Grant/Award Numbers: JFJC2021-047505-I, PID2022-136471N-B-C21&C22, PID2020-119651RB-I00; National Science Centre (Poland), Grant/Award Numbers: 2019/33/N/ST10/01479, 2014/14/ST10/00321; Foundation for Polish Science (FNP)

Handling Editor: Prof. Johann Diener

## Abstract

Aqueous fluids released during dehydration of a subducting slab have a large effect on the rheology of the subduction interface. While high-pressure experiments and natural-case studies link deformation with critical dehydration reactions during eclogitization, the exact interplay between these processes remains ambiguous. To investigate fluid–rock interaction and associated deformation at high-pressure, we studied a suite of eclogites from the Tsäkkok Lens of the Scandinavian Caledonides that record prograde metamorphism within an Early Palaeozoic cold subduction zone. Our results show that in-situ dehydration during the blueschist to eclogite facies transition produces fluid fluxes leading to rheological weakening and densification, consequently promoting ductile-brittle deformation. Petrographic evidence, supported by thermodynamic modelling and thermobarometry, attest to a prograde passage from lawsonite-blueschist to peak eclogite facies of ~2.5 GPa and ~620°C. Phengite-bearing eclogites imply interaction with an externally-derived fluid, whereas rare phengite-free, kyanite-eclogites only record internally-derived fluid production. Models predict that prograde breakdown of chlorite, lawsonite and amphibole between 500 and 610°C lead to progressive dehydration and release of up to 4.6 wt.% of aqueous fluid. Microstructural data reveal elongated shapes of highly strained omphacite porphyroblasts, displaying minor yet gradual changes in misorientation towards the grain boundaries. Occasionally, these intragranular structures form subgrain cells that have similar sizes to those of neoblasts in the rock matrix. These observations point to the potential onset of dynamic recrystallization processes via dislocation creep. Moreover, the omphacite neoblasts and rutile show non-random crystallographic preferred orientations (CPOs), which are characterized by the subparallel alignment of point-like maxima in rutile [001] and [100] axes to those of [001] and (010) of omphacite neoblasts, respectively. Additionally, the [001] axes of these minerals are also subparallel to the weak stretching mineral lineation, and the (100) of rutile and the (010) of omphacite neoblasts are distributed in the plane of the foliation. This suggests that the development of their

This is an open access article under the terms of the Creative Commons Attribution-NonCommercial License, which permits use, distribution and reproduction in any medium, provided the original work is properly cited and is not used for commercial purposes.
© 2024 The Authors. *Journal of Metamorphic Geology* published by John Wiley & Sons Ltd.

CPOs was coeval and structurally controlled. Garnet microfractures normal to the foliation are dilated and sealed predominantly by omphacite. The lack of obliquity between CPO and foliation plane, as well as the systematic orientation of garnet microfracture orientations, are consistent with coaxial deformation at peak-pressure conditions. Unlike other studies, we show that neither an external fluid source nor channelized fluid flow is needed to facilitate a ductile-brittle deformation of eclogite in a subduction setting.

**KEYWORDS**
EBSD, microstructure, pressure–temperature, Scandinavian Caledonides, seismicity, Seve Nappe Complex, subduction

## 1 | INTRODUCTION

Volatiles released from subducting slabs largely controls convergent margin processes, such as subduction zone seismicity (Peacock, 2001), mantle wedge mass transfer and convection (e.g., Arcay et al., 2005), as well as arc magmatism (Hawkesworth et al., 1993). At high-pressure conditions, hydrous fluids are produced during prograde dehydration of both the oceanic crust and lithospheric mantle portions of the subducting slab (Hacker et al., 2003). The fluid-producing reactions can be attributed to distinct facies changes, but the stability of the hydrous phases involved in the transition (thus, the absolute depths of dehydration) largely depends on the composition and thermal structure of the slab (Groppo & Castelli, 2010; Schmidt & Poli, 1998). Within the hydrated mantle part of the slab, the transition from antigorite-serpentinite to harzburgite is recognized to release a large amount of water (Padrón-Navarta et al., 2011; Scambelluri et al., 2004). In contrast, within the oceanic crust part of the slab, the blueschist to eclogite facies transition is critical as it is associated with significant metamorphic dehydration reactions (Hacker et al., 2003 and references therein).

The association of seismicity with the dehydrating regions of a slab (Peacock, 2001 and references therein) has stimulated multiple studies investigating the dehydration of rock volumes in the subducting slab. (Ultra)high-pressure low-temperature ([U]HP-LT) rocks attracted the most attention, as brittle or brittle-ductile deformation (potentially related to seismic events) is prone to occur at low-temperature conditions. Natural case studies of HP-LT deformation report pseudotachylytes (Austrheim & Boundy, 1994; John & Schenk, 2006; Scambelluri et al., 2017), cataclasites and eclogite-facies breccias (Angiboust et al., 2012; Hertgen et al., 2017; Yang et al., 2014), and often attribute it to fluid presence, largely affecting the mechanical properties of rocks (Boland & Tullis, 1986; Putnis et al., 2018). However, the cause of brittle failure and the exact role of fluid during (U)HP-LT deformation remain highly debated. Deformation models related to dehydration invoked pore-fluid overpressure, leading to dehydration embrittlement as a primary mechanism (Hacker et al., 2003; Jung et al., 2004). However, other studies supported transformational faulting processes (Kirby, 1987; Schubnel et al., 2013), grain size reduction (Incel et al., 2017; Thielmann et al., 2015) and thermal runaway (John et al., 2009; Thielmann, 2018), or spatially heterogenous dehydration causing dehydration-driven stress transfer (Ferrand et al., 2017). Although the underlying mechanisms remain unclear, a strong link exists between the dehydration reactions during prograde eclogitization and brittle or brittle-ductile deformation of potentially seismic origin.

This paper presents a comprehensive petrological and microstructural study of eclogites from the Tsäkkok Lens in the Scandinavian Caledonides. We combine a set of thermobarometrical methods with electron backscatter diffraction (EBSD) to reconstruct the pressure–temperature-deformation (P–T-d) path, reaching conditions of approximately 2.5 GPa and 620°C. We investigate the prograde transition from blueschist to eclogite facies, with particular emphasis on the metamorphic dehydration processes associated with chlorite, lawsonite and amphibole breakdown, as well as the consequential rheological changes induced by the release of fluids. These results demonstrate the interplay between dehydration and deformation in high-pressure rocks, which presumably can be linked with intermediate-depth seismicity observed in cold subduction zones.

## 2 | GEOLOGICAL SETTING

The Tsäkkok Lens is located in northern Sweden (Norrbotten region). It belongs to the Seve Nappe Complex (SNC), which represents the upper part of the Middle Allochthon of the Scandinavian Caledonides (Figure 1a; Gee et al., 2013). The Scandinavian Caledonides originate from the early Palaeozoic closure of the Iapetus Ocean and

15251314, 0, Downloaded from https://onlinelibrary.wiley.com/doi/10.1111/jmg.12765 by Universidad De Granada, Wiley Online Library on [11/04/2024]. See the Terms and Conditions (https://onlinelibrary.wiley.com/terms-and-conditions) on Wiley Online Library for rules of use; OA articles are governed by the applicable Creative Commons License

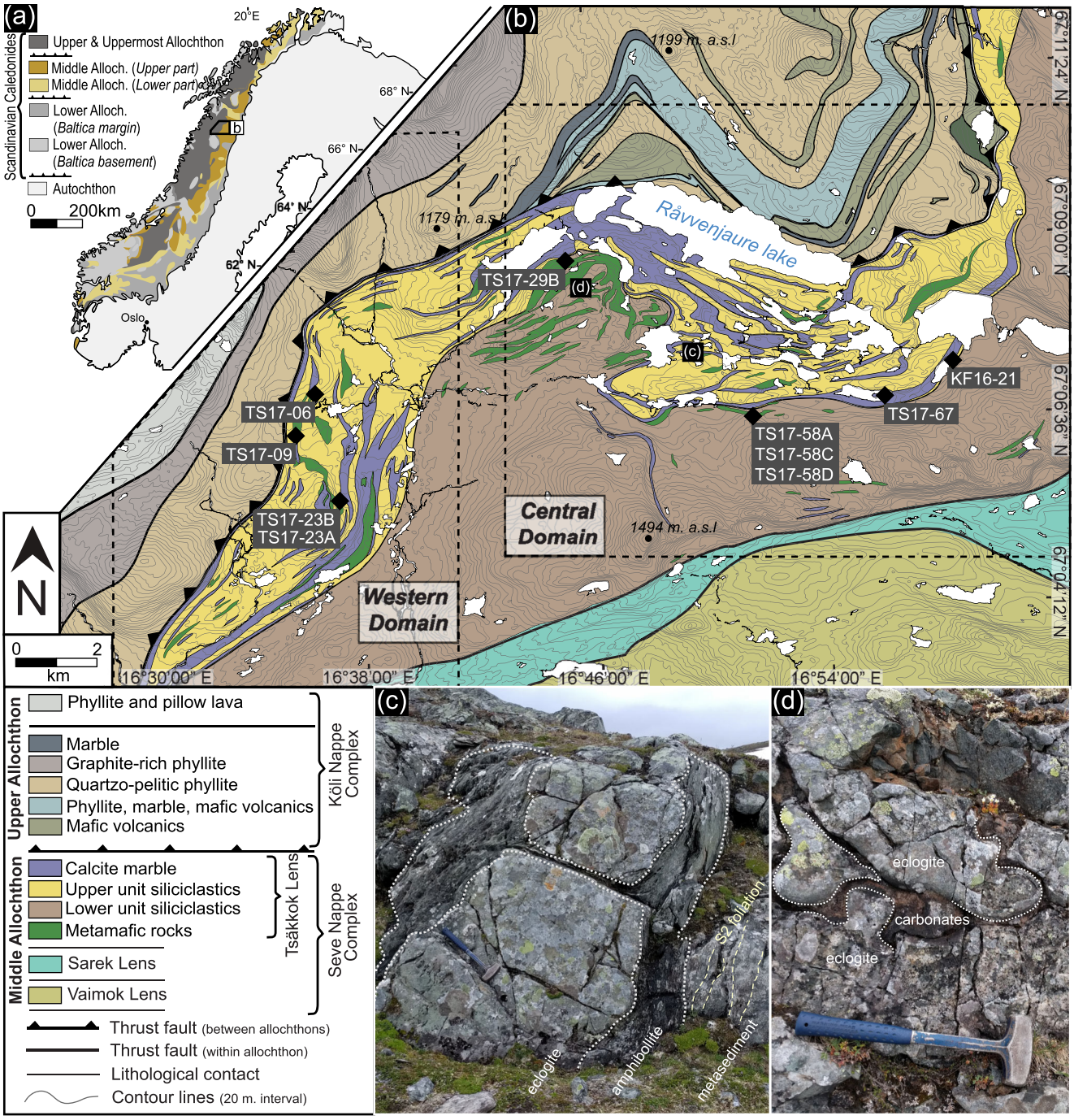


**FIGURE 1** Geological map and eclogite outcrops. (a) Simplified tectonostratigraphic map of the Scandinavian Caledonides (after Gee et al., 2013). Black polygon indicates the location of the study area. (b) Tectonostratigraphic map of the Tsäkkok Lens with adjacent units (modified after Barnes et al., 2020, and references therein). Black diamonds indicate the location of outcrops and samples. Dashed polygons show the extent of the western and central domains. (c) Field photograph of a representative outcrop of an eclogite lens enveloped by amphibolite with foliation concordant to the S2 foliation of host metasedimentary rocks. (d) Eclogite with a pillow lava shape.

subsequent collision of Laurentia and Baltica (e.g., Andréasson et al., 1985; Stephens & van Roermund, 1984). The Middle Allochthon is classically regarded to represent the outer margin of Baltica. The SNC is traditionally interpreted as a dyke-intruded passive margin sedimentary succession (Gee et al., 2013), but an outboard terrane origin has also been discussed (e.g., Corfu et al., 2014).

The exposure of the SNC in Norrbotten (Figure 1a) is dominated by non-migmatitic siliciclastic metasedimentary rocks and marbles hosting lenses of eclogites and garnet (±spinel) ultramafics (Andréasson, 1987; Kullerud, 1987; Van Roermund, 1989). An increasing number of geochronological reports on the SNC in Norrbotten collectively suggest a Neoproterozoic maximum

15251314, 0, Downloaded from https://onlinelibrary.wiley.com/doi/10.1111/jmg.12765 by Universidad De Granada, Wiley Online Library on [11/04/2024]. See the Terms and Conditions (https://onlinelibrary.wiley.com/terms-and-conditions) on Wiley Online Library for rules of use; OA articles are governed by the applicable Creative Commons License

deposition age of metasedimentary protoliths (Barnes, Majka, Bukała, et al., 2021), a c. 600 Ma age of mafic rocks (Root & Corfu, 2012; Svenningsen, 2001) and a Cambrian/Early Ordovician age of peak metamorphism (Barnes, Majka, Jeanneret, et al., 2021; Fassmer et al., 2021; Mørk et al., 1988; Root & Corfu, 2012). The SNC is tectonically overlain by an Iapetus-derived Upper Allochthon (Figure 1b).

The Tsäkkok eclogites have a tholeiitic composition with an E-MORB signature (Kullerud et al., 1990), some of which are former pillow basalts. The Tsäkkok Lens represents the only fragment of the SNC where pristine glaucophane in (retro)blueschists have been found. The first published P–T estimates yielded a minimum pressure of 1.50 GPa at 500–630°C (Kullerud et al., 1990). Recent studies reported mesoscale brittle fracturing events to occur at ~2.45 GPa and ~620°C (Bukała et al., 2020), close to peak conditions of 2.50–2.60 GPa at 590–664°C obtained by conventional thermobarometry (Fassmer et al., 2021). The timing of peak metamorphism varies depending on the method from 503 ± 18 Ma (garnet Sm–Nd; Mørk et al., 1988) to 481.9 ± 1.2 Ma (zircon U–Pb; Root & Corfu, 2012). The latter seems more favourable since Fassmer et al. (2021) obtained the age of prograde metamorphism between 487.7 ± 4.6 and 484.6 ± 4.6 Ma (garnet Lu-Hf). Kullerud (1987) distinguished two Tsäkkok subunits and recognized three deformation events. The Lower Unit is dominated by quartzofeldspathic gneisses and garnet-bearing mica schists, and the Upper Unit is composed of marbles, calcareous schists and garnet-bearing mica schists. The subduction-related S1 foliation, denoting the prograde-to-peak metamorphic stages, is rarely preserved. The early D2 event denotes coaxial deformation related to exhumation from HP conditions (477.2 ± 4.1 to 475.3 ± 3.5 Ma), whereas late D2 resulted from non-coaxial vertical shortening that might have proceeded until 458.1 ± 9.0 Ma; and the last stage, D3, relates to NE–SW shortening during thrusting at 429.9 ± 9.0 Ma (Barnes et al., 2020). Since the interior of eclogite bodies was sheltered from retrograde alteration, the Tsäkkok eclogites provide a unique opportunity to study the HP-LT processes operating within a cold, Early-Palaeozoic subduction zone.

## 3 | SAMPLING STRATEGY AND ANALYTICAL TECHNIQUES

### 3.1 | Outcrop description and sampling strategy

A set of 50 eclogite samples was collected throughout the Tsäkkok Lens, mostly within its western and central domains. Tsäkkok Lens presents challenges for field structural analysis. Intermittent outcrop exposure hinders observations on a tens-of-meters scale, making precise tracing of the extent and contact between different eclogite types difficult. Poor rock exposure quality, primarily due to extensive lichen and snow coverage, renders macro-scale documentation of LS-fabric and stretching lineation orientations nearly unattainable at the outcrop scale. The metabasic rocks occur as lenses, boudins and layers elongated concordantly to the exhumation-related S2 foliation of the host metasedimentary rocks of the Lower and Upper Units (Figure 1b). The metabasite bodies vary in length from centimetres to >250 m and often display internal zoning. Massive cores consist of fresh and seemingly undeformed eclogite that show only minor retrograde alteration. Sporadically, the weak foliation and lineation can be traced within the cores of the eclogite bodies that are composed of Ph-bearing eclogites, where the alignment of stretched white mica flakes defines a weak fabric. An outer zone is dominated by amphibole- and greenschist-facies assemblages that define late foliations parallel to the surrounding S2 foliation (Figure 1c). Within the largest bodies (>50 m) the eclogite preserves a pillow lava fabric (Figure 1d; Kullerud, 1987, Bukała et al., 2020, Fassmer et al., 2021). Locally, eclogite outcrops show networks of mesofractures and veins sealed either by garnet or omphacite, that are interpreted as fluid migration pathways (Bukała et al., 2020).

A set of 10 samples with well-preserved eclogite-facies assemblages were chosen for further petrographic and chemical analyses (Table S1). Out of these, three eclogites, i.e., non-foliated (TS17–67), weakly foliated (TS17–58D) and moderately foliated (KF16–21), were chosen for microstructural analysis. In samples, KF16–21 and TS17–58D – the only eclogites with a macroscopically visible foliation defined by the alignment of white mica – thin sections were cut perpendicular to the foliation plane and parallel to weak lineation. In other samples, the thin sections were not oriented and cut solely according to the best preservation of eclogite-facies minerals.

### 3.2 | Electron microprobe (EMP)

Mineral chemistry was analysed in wavelength dispersive spectrometry (WDS) mode using a JEOL Superprobe 8,230 EMP at AGH University of Science and Technology (AGH-UST, Poland), and a JEOL JXA8530F Hyperprobe FEG Electron Probe Microanalyser at Uppsala University (UU, Sweden). The conditions for silicate mineral analyses were: an accelerating voltage of 15 kV and a beam current of 15–20 nA. The counting times were 20 s on peaks and 10 s on background positions. The beam size ranges from 1 to 15 μm depending on the mineral. For

15251314, 0, Downloaded from https://onlinelibrary.wiley.com/doi/10.1111/jmg.12765 by Universidad De Granada, Wiley Online Library on [11/04/2024]. See the Terms and Conditions (https://onlinelibrary.wiley.com/terms-and-conditions) on Wiley Online Library for rules of use; OA articles are governed by the applicable Creative Commons License

the rutile analyses (AGH-UST), an accelerating voltage of 15 kV and beam current of 120 nA were used with counting times of 150–300 s on peaks and 75–150 s on background positions. Additional standards used for rutile analyses: zircon (Zr), $LiNbO_3$ (Nb) and tantalite-(Mn) (Ta). The JEOL JXA8530F Hyperprobe was used to collect WDS X-ray maps using a 70 nA beam current, a 15 kV accelerating voltage and a 75 ms dwell time with a 1 μm grid step. The JEOL JXA8530F Hyperprobe was used to collect WDS X-ray maps using a 40 nA beam current, a 15 kV accelerating voltage and a 150 ms dwell time with a 0.5 μm grid step.

Amphibole analyses were recalculated using the spreadsheet of Locock (2014) and named according to Hawthorne et al. (2012). The ferric iron content in garnet and clinopyroxene has been estimated using the stoichiometric method from Droop (1987). Mineral abbreviations are after Whitney and Evans (2010), with an additional one for white mica - WM.

## 3.3 | Bulk rock composition

The bulk rock composition of 10 eclogite samples (Table S2) was analysed by ICP-ES at the Bureau Veritas Mineral Laboratories in Canada. The detection limits for major elements were: $SiO_2$, $Al_2O_3$, $K_2O$, MgO, MnO, $Na_2O$, $P_2O_5$, $TiO_2$ - 0.01 wt.%, $Cr_2O_3$ - 0.002 wt.%, $Fe_2O_3$ - 0.04 wt.%, and for trace elements: Ba, Nb, Zr - 5 ppm, Y - 3 ppm, Sr - 2 ppm, Sc - 1 ppm.

## 3.4 | Electron backscatter diffraction (EBSD)

Phase and orientation mapping by EBSD were conducted under low vacuum (at 10 Pa) in a Zeiss EVO MA 15 Scanning Electron Microscope at the Instituto Andaluz de Ciencias de la Tierra (Armilla, Spain), equipped with an Oxford Instruments Nordlys Nano EBSD detector. The instrument was set to a 20 kV acceleration voltage, a 24 mm working distance and a probe current of up to 500 pA. The settings in the Aztec v. 3.1 (Oxford/HKL) data acquisition software were 4 × 4 binning and a low (0) gain with a grid step of 19 μm for large area mapping of entire thin sections and 5–6 μm for detailed maps.

### 3.4.1 | Data processing

The percentage of indexed points in the raw maps exceeded 85% and only minor post-processing was necessary using the built-in functions of the Oxford/HKL Channel 5 software package by removing wild spikes and filling non-indexed pixels based on the orientations of six neighbouring pixels. Further data processing and calculations were accomplished using the MTEX 5.2.7 Matlab toolbox (https://mtex-toolbox.github.io; Hielscher & Schaeben, 2008; Bachmann et al., 2010). Grains were reconstructed with the 'calcGrains' function using a segmentation angle of 12° between neighbouring pixels. For the initial evaluation of a suitable method for reconstructing omphacite microstructures and differentiating neoblasts from porphyroblasts, we tested cut-offs based on grain-size, and grain orientation spread (GOS; presented later) criteria. In the sample with the strongest fabric (TS17-67), a GOS-based method effectively differentiated high-GOS porphyroblasts from low-GOS neoblasts. However, in samples with a weaker fabric (TS17-58D, KF16-21), the close crystallographic orientation of certain larger neoblasts led to their artificial coalescence in the EBSD maps. This resulted in the appearance of artificial subgrain boundaries (checked using optical microscopes) and an unusually high GOS at the sample scale despite a consistent correlation of the overall average grain size, shape-preferred orientation (SPO) and crystallographic-preferred orientation (CPO) with neoblasts rather than with porphyroblasts. Considering the results of both methods, the grain size criterion was deemed more reliable thus an equivalent diameter (ED) cut-off value was applied for an accurate reconstruction of the observed microstructure. Grains with ED < 350 μm (KF16-21, TS17-58D) and <300 μm (TS17-67) were classified as neoblasts. The SPO of matrix grains is expressed as the orientation of the long axis of the fitted ellipse in each grain with respect to a horizontal line corresponding to 0°. The orientation of garnet microfractures has been measured on wide-open microfractures. Misorientation (Mis2Mean) is calculated as the misorientation of a pixel within a grain relative to the mean orientation of the same grain and is expressed in degrees. The GOS is calculated in each grain as the simple average of Mis2Mean values. More information on these parameters is available in Wright et al. (2011). Inverse pole figure (IPF) maps are colour-coded with respect to the x-vector (oriented parallel to the long side of thin sections). Due to bimodal omphacite grain size distribution, contoured pole figures are constructed based on the one-point-per-grain data (OPPG) to avoid the over-representation of large grains.

### 3.4.2 | Crystallographic preferred orientation (CPO)

Traditionally, the distinction of tectonite fabric relies on SPO analyses, with two end-members of S-tectonites

15251314, 0, Downloaded from https://onlinelibrary.wiley.com/doi/10.1111/jmg.12765 by Universidad De Granada, Wiley Online Library on [11/04/2024]. See the Terms and Conditions (https://onlinelibrary.wiley.com/terms-and-conditions) on Wiley Online Library for rules of use; OA articles are governed by the applicable Creative Commons License

(corresponding to oblate ellipsoid; uniaxial flattening) and L-tectonites (prolate ellipsoid; uniaxial stretching). However, given the uncertainties with thin section orientation, hence, possibly unreliable SPO, the CPO-based method has been utilized. The CPO of omphacite has been quantified using the LS-index (Ulrich & Mainprice, 2005). This method relies on eigenvalue analysis of the (010) and [001] pole figure symmetry. A normalized LS-index varies between 0 and 1 representing a spread between S-type (LS-index ≈ 0) and L-type (LS-index ≈ 1) fabric endmembers. In the context of deformation, the S-type fabric usually indicates axially symmetric compression, and the L-type fabric develops in axially symmetric extension, while the mixed LS-type (intermediate LS-index) is consistent with simple- or pure-shear (Ulrich & Mainprice, 2005).

# 4 | PETROGRAPHY, GEOCHEMISTRY AND MICROSTRUCTURES

## 4.1 | Types of eclogites: lithology and whole rock geochemistry

The Tsäkkok eclogites show a range of subtypes and overprinting mineral assemblages that record consecutive metamorphic stages along the clockwise P–T path. Among the eclogites that preserve unaltered eclogite facies assemblages, the two most prominent types are phengite-free (Ph-free) and phengite-bearing (Ph-bearing) eclogites. Both can be found within a single eclogite lens (e.g., outcrop TS17-58; Figure 1b and Table S2), however, no systematic spatial relationship between these types has been observed. The Ph-free eclogites are rare and preserve a high-P assemblage of Grt + Omp + Rt + Qz ± Ky. This type is represented by sample TS17-67, a non-foliated eclogite with fine-grained granoblastic texture (Figure 2a). In contrast, the common Ph-bearing eclogites contain an assemblage of Grt + Omp + Ph + Rt + Qz. This type is represented by samples TS17–58D, a weakly-foliated eclogite showing a fine- to medium-grained granoblastic texture (Figure 2b), and KF16–21, a moderately-foliated eclogite with a fine- to medium-grained nematoblastic texture (Figure 2c). Additionally, minor amounts of apatite, zircon and carbonate may occur in both types.

The difference between the Ph-free and Ph-bearing eclogites is also reflected in the bulk composition. The Ph-free eclogites show low content of fluid-mobile, Large-Ion Lithophile Elements (LILE) with concentrations of $K_2O$ < 0.13 wt.% and Ba < 60 ppm (Figure 3). Contrarily, the Ph-bearing eclogites display higher values of $K_2O$ (>0.36 wt.%) and Ba (>125 ppm). Only the Sr content for the two eclogite groups shows minor overlap with values of <184 ppm in Ph-free and >163 ppm in Ph-bearing types (Table S2).

## 4.2 | Petrography, microstructures and mineral geochemistry

Three key samples (TS17-67, TS17-58D, KF16-21) show similar petrographic and microstructural features. A detailed information is provided in Supplementary Materials. For ease of comparison, the numbering provided as the subscript suffixes of each phase (e.g., $Omp_1$) designates the generation for each mineral that formed during consecutive metamorphic stages (Figure 4; cf. Section 6.1).

### 4.2.1 | Garnet

Garnet forms either single idiomorphic to hypidiomorphic porphyroblasts (Figure 5a), or clusters of several amalgamated grains surrounded by a single, continuous rim (Figure 5b, Bukała et al., 2020). It displays zoning with the core ($Grt_1$) preserving a prograde compositional change characterized by a rimward decrease of Fe and Mn compensated by an Mg increase (Figure 6a; Figure S2). Ca often shows a patchy distribution, slightly decreasing towards the rim. The contact between the core and rim is sharp and denoted by an abrupt increase in Mg content and a decrease in Fe, Ca and Mn. The rim ($Grt_2$) has a homogenous, high-Mg composition. Subtle Mn oscillatory zoning has been observed within some garnet rims (Figure S2). The chemical zoning is often disrupted by a network of high-Mg microchannels propagating outward from polyphase inclusions of Czo ± Qz ± Ky ± Pg (interpreted as Lws-pseudomorphs), and penetrating through both core and rim (not presented here; see Bukała et al., 2020). Even though the garnet interior is virtually undeformed, low-angle (<3°) boundaries can be traced along some microchannels. A detailed description of microchannels and intracrystalline misorientation has been reported by Bukała et al. (2020). Garnet porphyroblasts and garnet clusters are locally dismembered. Microfractures separating garnet fragments are up to 300 μm wide and sealed by the HP assemblage of Omp ± Qz ± Ph (Figure 5b,c). Microfractures (Figure 2) in Ph-bearing samples are oriented either perpendicular or slightly oblique to the foliation denoted by the SPO of omphacite, rutile and phengite. In contrast, garnet microfractures in the Ph-free sample are oriented at <54° to the mean SPO of omphacite neoblasts and show a larger spread of orientations (Figure 2). Garnet inner cores host

15251314, 0, Downloaded from https://onlinelibrary.wiley.com/doi/10.1111/jmg.12765 by Universidad De Granada, Wiley Online Library on [11/04/2024]. See the Terms and Conditions (https://onlinelibrary.wiley.com/terms-and-conditions) on Wiley Online Library for rules of use; OA articles are governed by the applicable Creative Commons License

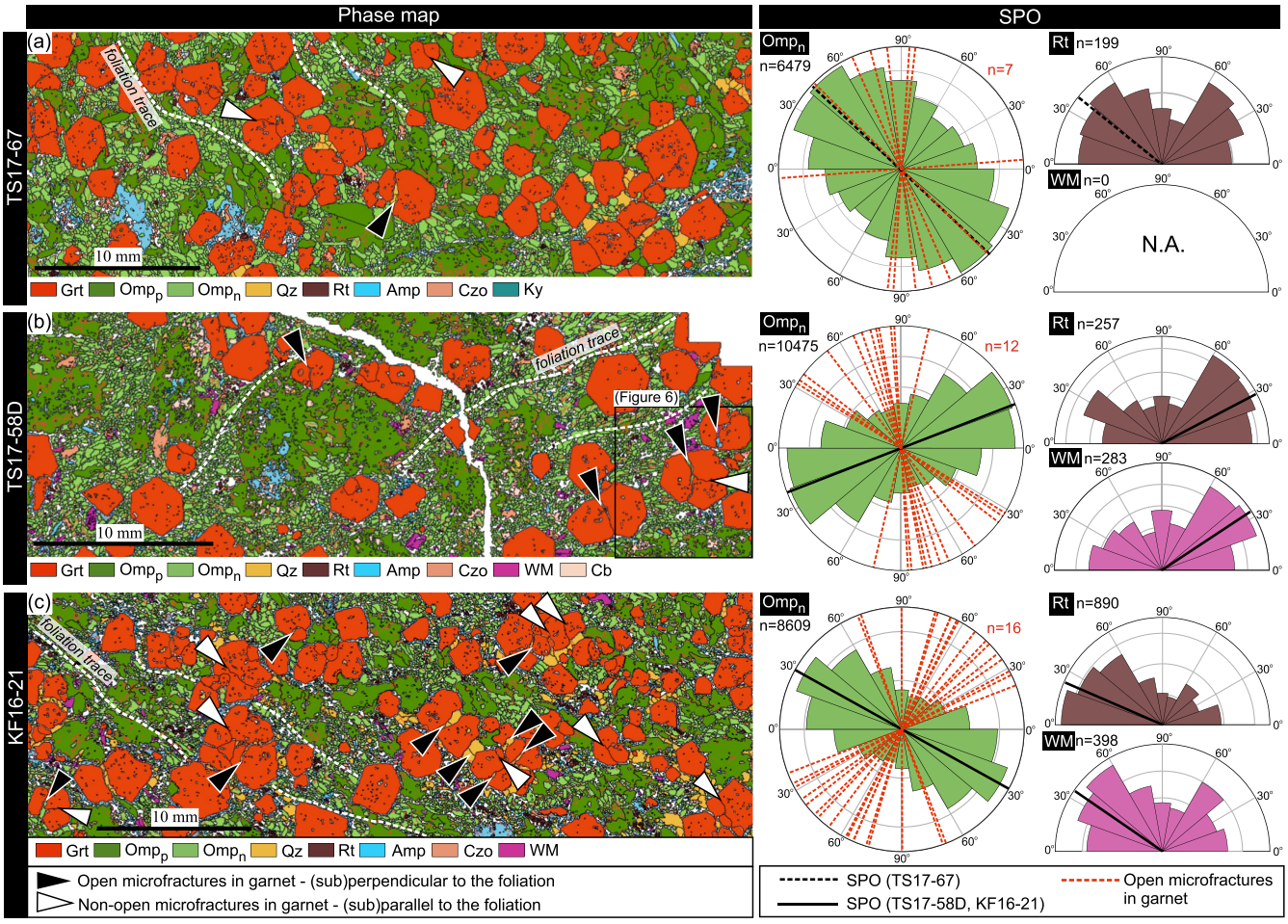


**FIGURE 2** EBSD phase maps of representative eclogite samples and shape preferred orientation (SPO) of major phases in the thin section frame. (a, c, e) phase maps of representative areas of non-foliated TS17–67, weakly-foliated TS17–58D and moderately-foliated KF16–21 eclogites, respectively. The black rectangle marks the location of the high-resolution EBSD map presented in Figure 7. Black triangles point to wide-open microfractures in garnet ([sub]perpendicular to foliation), whereas white triangles indicate non-open microfractures ([sub]parallel to foliation). (b, g, m) rose diagrams showing the SPOs of omphacite (green), rutile (brown) and white mica (purple). The black solid line (TS17–58D and KF16–21) and dashed line (TS17–67) indicate the mean orientation of each phase. The mean orientation of all phases points in a similar direction within each sample, denoting the trace of the foliation. Note that this foliation is not visible in hand specimen of the non-foliated TS17–67 eclogite, presented in (a). The dotted red lines superimposed on the omphacite SPOs show orientation of wide-open garnet microfractures. N.A. - non-analysed.

numerous monophase inclusion of (Na-Ca)-amphibole, (Na)-amphibole, omphacite, rutile, quartz, chlorite and Lws-pseudomorphs (Figure 5d). Garnet outer cores and rims contain rare omphacite and rutile inclusions only.

### 4.2.2 | Clinopyroxene

Clinopyroxene of omphacite composition records three chemical generations varying in $X_{Jd}$ and $X_{Aeg}$. Omphacite predominantly forms large, xenomorphic porphyroblasts ($Omp_p$) surrounded by swarms of small, prismatic neoblasts ($Omp_n$). The neoblasts, along with phengite and rutile, define a weak foliation slightly anastomosing around garnet and omphacite porphyroblasts in the Ph-bearing eclogites (Figure 2). Despite the size difference, porphyroblasts and neoblasts show similar chemical zoning. The core ($Omp_1$) of highly irregular shape and lobate boundaries is overgrown by a rim ($Omp_2$; Figure 5e,f). Even though the composition of $Omp_1$ is heterogeneous and characterized by a patchy distribution of Fe (Figures 5f and 6), Na, Ca and Mg (Figure S1), it represents an overall higher-$X_{Aeg}$ generation (Figure 6b). The high- to low-$X_{Aeg}$ omphacite transition in some samples is not well pronounced, but the overall trend in rimward Fe depletion can be traced (Table S4).

Omphacite within garnet microfractures forms grains closely sealing the fracture (Figures 5b and 7g,h) and

15251314, 0, Downloaded from https://onlinelibrary.wiley.com/doi/10.1111/jmg.12765 by Universidad De Granada, Wiley Online Library on [11/04/2024]. See the Terms and Conditions (https://onlinelibrary.wiley.com/terms-and-conditions) on Wiley Online Library for rules of use; OA articles are governed by the applicable Creative Commons License

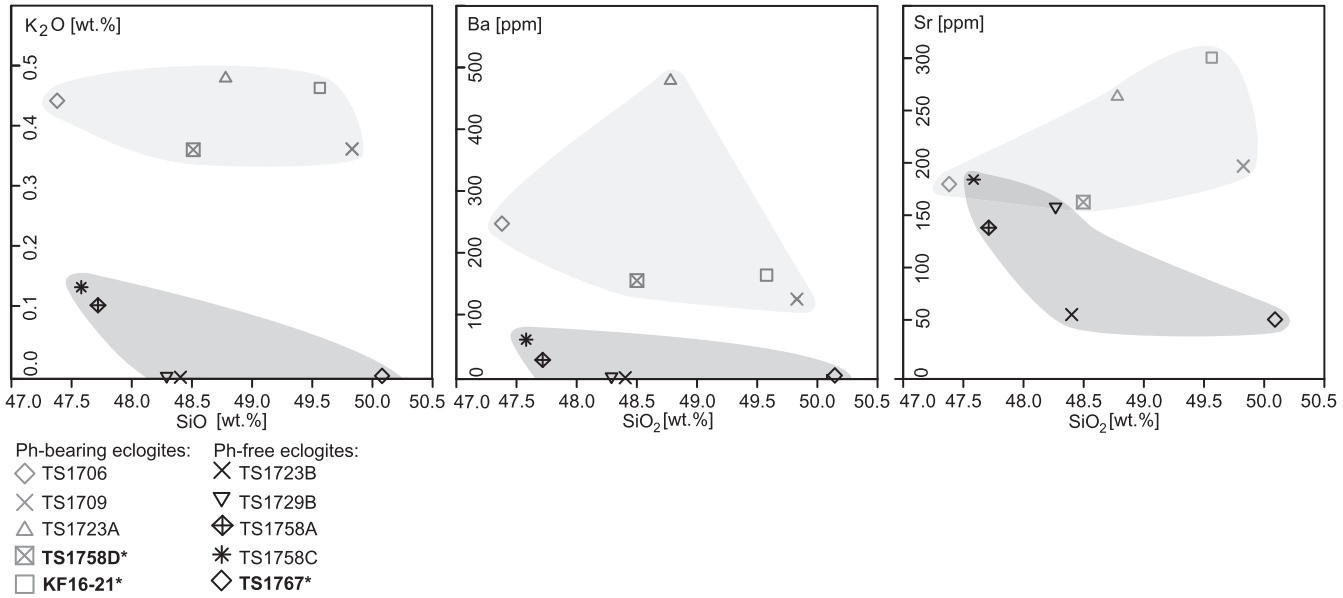


**FIGURE 3** Bulk rock composition of Ph-bearing and Ph-free eclogites (* samples studied in detail).

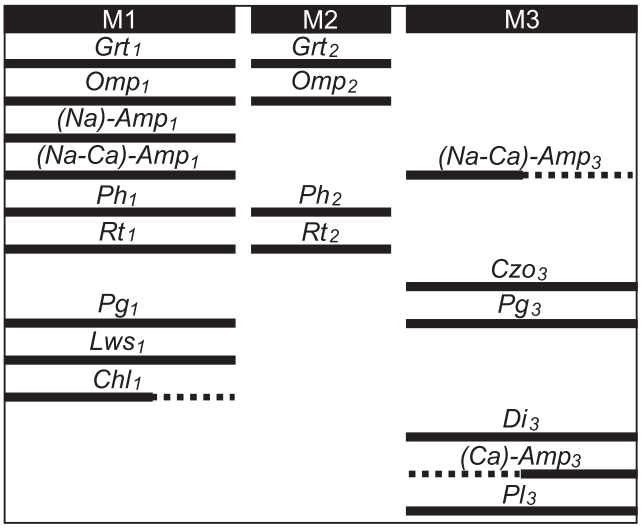


**FIGURE 4** Mineral assemblages. The dotted line indicates presumed presence during the early/late stage of mineral assemblage formation.

shows a high-$X_{Jd}$ composition similar to the $Omp_2$ composition (Figure 6b). Omphacite also forms common monophase and rare polyphase (Omp ± (Na)-Amp ± Qz ± Rt) inclusions in garnet. The composition of omphacite inclusions varies over a broad range, yet due to distinct high-$X_{Aeg}$ content, it resembles $Omp_1$ (Figure 6b). Clinopyroxene of diopside composition is associated with (Ca)-Amp ± Ab ± Qz symplectites surrounding omphacite porphyroblasts or within a Pg ± Di ± Qz assemblage within a porphyroblast interior (Figure S4).

The omphacite porphyroblasts form hypidiomorphic grains exceeding 1.5 mm of equivalent diameter, whereas the neoblasts have a mean of ~120 μm (Figure 2 and Figure S3). Porphyroblasts are highly strained and a rimward increase of lattice distortion is attested either by a gradual or sharp increase of misorientation (Figure 7d), while the lattice rotations are consistently accommodated by dislocation activity around [010] and [001] axes, with only minor differences between samples (Figures 7 and 8). Occasionally, near the edges of omphacite porphyroblasts, subgrain cells are found (Figure 7) that have similar sizes to those of neoblasts in the rock matrix (Figure S3). The strain difference between porphyroblasts and neoblasts is expressed by a drop of GOS by ~55%. The neoblasts in Ph-bearing samples show a strong SPO with one dominant direction (>70% of grains) parallel to the foliation, whereas the Ph-free sample displays a weak SPO with one direction. The spread of remaining grains in Ph-bearing samples reflects the orientation of fine-grained matrix anastomosing around porphyroblasts (Figure 2).

In all samples, the CPO of omphacite porphyroblasts shows a nearly random distribution (Figure 9). However, the (010) and [001] pole figures display weak, irregularly shaped maxima roughly correlating with maxima on corresponding pole figures of neoblasts. The (010), (110) and [001] neoblasts show blurred point-like maxima connected by poorly defined girdles (Figure 9). In the Ph-bearing samples, the orientation of the omphacite [001]-axis correlates with the SPO defined by the elongation of omphacite neoblasts and phengite. In contrast, provided the out-of-plane orientation of [001]-axis in the Ph-free

15251314, 0, Downloaded from https://onlinelibrary.wiley.com/doi/10.1111/jmg.12765 by Universidad De Granada, Wiley Online Library on [11/04/2024]. See the Terms and Conditions (https://onlinelibrary.wiley.com/terms-and-conditions) on Wiley Online Library for rules of use; OA articles are governed by the applicable Creative Commons License

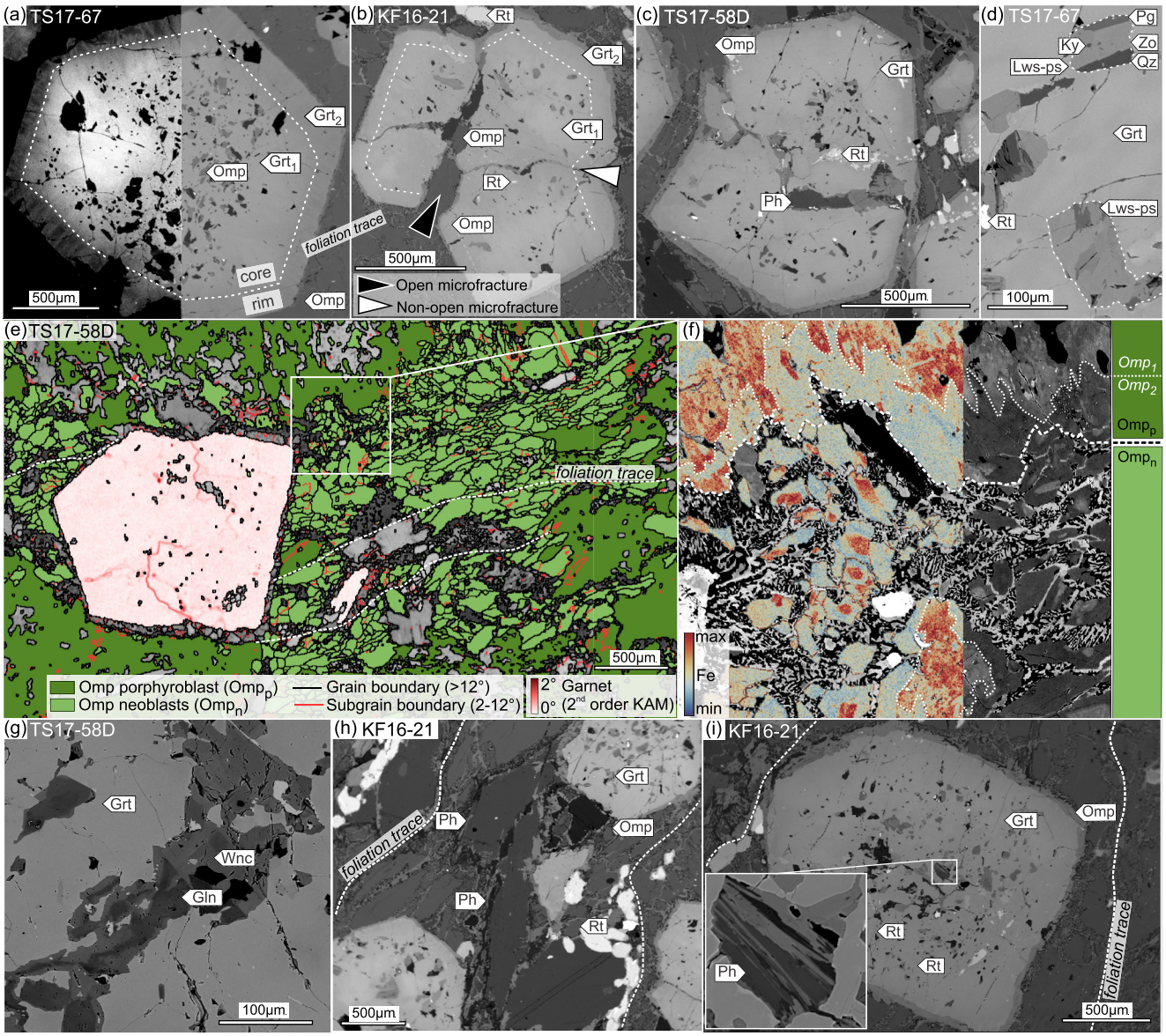


**FIGURE 5** Backscattered electron (BSE) images and WDS map showing petrographic features of eclogites. (a) Idiomorphic garnet displaying core ($Grt_1$) - rim ($Grt_2$) transition. The high-contrast BSE image shows that primary composition is disrupted along microchannels (cf. Figure S2). (b) Cluster of amalgamated garnet cores surrounded by a single, continuous rim. The microfracture is sealed by a single crystal of omphacite. (c) Fractured garnet sealed by phengite. (d) Rhomboidal Lws-pseudomorphs in garnet. (e) EBSD data showing phase map of omphacite porphyroblasts (dark green) and neoblasts (bright green), and second nearest-neighbour Kernel Average Misorientation (second order KAM) map of garnet porphyroblast. Note: (i) the two low-angle misorientation populations in garnet, both oriented perpendicular to the foliation and (ii) the sharper low-angle boundaries at the edge of the porphyroblast compared to the grain interiors, where changes in misorientations are more gradual and diffuse (cf. Bukała et al., 2020). Grey background shows band contrast of all indexed phases except garnet and omphacite within selected area from the weakly-foliated TS17–58D eclogite. (f) Close-up Fe X-ray map (left) and BSE image (right) at the contact between omphacite porphyroblasts and neoblasts; enlarged from (e). The $Omp_1$ (core) and $Omp_2$ (rim) notations refer to the chemical zones within omphacite (thin dotted line), while the porphyroblast ($Omp_p$) and neoblast ($Omp_n$) terminology reflects the textural position of omphacite (thick dashed line). (g) Inclusions of (Na)-Amp1 (Gln, glaucophane) and (Na-ca)-Amp1 (Wnc, winchite) within the garnet core. (h) Large phengite ($Ph_2$) grains, omphacite neoblasts and rutile concordant to the foliation. (i) Phengite ($Ph_1$) inclusions within the garnet core ($Grt_1$). For the complete list of metamorphic mineral assemblages, see Figure 4.

sample, we conclude that observed SPO is caused by the oblique intersection of a thin-section plane to the weak foliation denoted by the CPO. Therefore, the SPO in the TS17–67 sample does not reflect the elongation direction and will no longer be discussed. Hence, in all samples, the omphacite neoblasts [001] are oriented parallel to the

15251314, 0, Downloaded from https://onlinelibrary.wiley.com/doi/10.1111/jmg.12765 by Universidad De Granada, Wiley Online Library on [11/04/2024]. See the Terms and Conditions (https://onlinelibrary.wiley.com/terms-and-conditions) on Wiley Online Library for rules of use; OA articles are governed by the applicable Creative Commons License

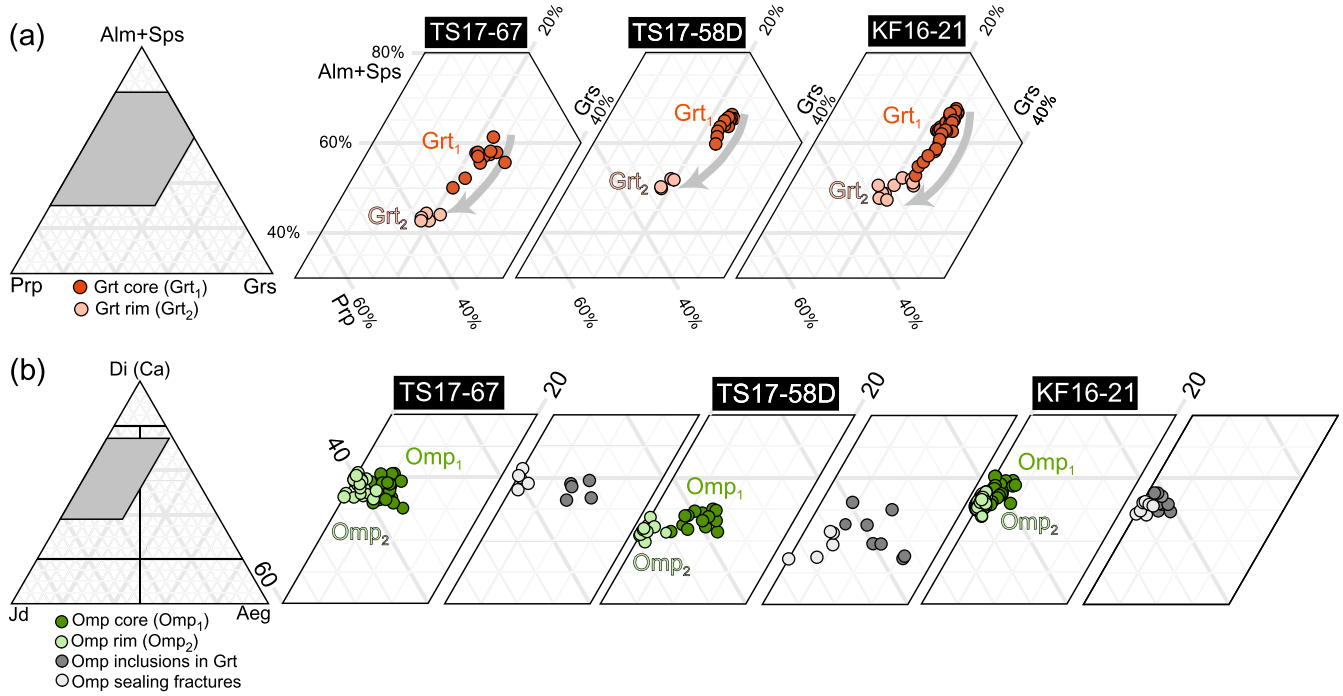


**FIGURE 6** Chemical compositions of garnet and omphacite. (a) Ternary diagrams present changes within the garnet core ($Grt_1$) and the difference between core and rim ($Grt_2$). Note that garnet in all the three eclogite samples show the same trend despite the differences in composition. (b) Chemistry of omphacite clinopyroxene following the classification of Morimoto et al. (1988).

foliation, whereas the (010) and (110) are normal to the foliation. Noteworthy, the orientation of omphacite sealing garnet microfracture mimics the nearby matrix-located neoblasts. The [001] axis is oriented perpendicular or slightly oblique to the microfracture walls (Figure 7g,h).

The LS-index of omphacite neoblasts increases with respect to porphyroblasts (TS17–67: 0.37 → 0.67, TS17–58D: 0.45 → 0.54 and KF12–21: 0.50 → 0.60). The interpretation of the LS-index of porphyroblasts is difficult due to predominantly random CPOs possibly inherited from an igneous precursor. However, the omphacite neoblasts collectively show an intermediate LS-index.

### 4.2.3 | Amphibole

Amphibole occurs in four textural positions. Inclusions hosted in garnet core ($Grt_1$) belong either to (Na-Ca)-amphibole ((Na-Ca)-$Amp_1$: taramite, winchite and katophorite) or (Na)-amphibole group ((Na)-$Amp_1$: glaucophane; Figure 5g). Strain-free amphibole in the matrix, or replacing the strongly deformed cores of omphacite porphyroblasts, belongs to (Na-Ca)-amphibole ((Na-Ca)-$Amp_3$: winchite and katophorite), however, the composition of some matrix grains shows core-to-rim zoning from winchite to katophorite (Figure S4). Amphibole forming symplectites after omphacite and rims around the garnet display a (Ca)-amphibole composition ((Ca)-$Amp_4$: pargasite, sadanagaite or actinolite). The CPO of amphibole mimics that of omphacite in sample KF16-21, whereas the other samples show only weak correlation and nearly random distribution. The point-like maxima of the amphibole [001] and (010) are weakly defined and dispersed (Figure 9).

### 4.2.4 | White mica

White mica predominantly forms grains located within the fine-grained matrix of the Ph-bearing eclogites. It shows a moderate SPO with a main direction parallel to the foliation and is oriented along the grain boundaries of omphacite neoblasts (Figure 2). Both phengite and paragonite grains are adjacent to each other. However, the paragonite grains ($Pg_1$) are partially decomposed and exhibit lobate boundaries surrounded by Amp ± Czo ± Qz ± Pl intergrowths. Also, while most paragonite grains are concordant to the foliation, numerous discordant paragonite grains are readily observed (Figure S4). The phengite grains ($Ph_2$) do not show signs of breakdown and are concordant to the foliation (Figure 5h). Additionally, phengite is localized in the garnet microfractures ($Ph_2$; Figure 5c). A phengite inclusion ($Ph_1$) in garnet has been observed only in one porphyroblast (KF16–21; Figure 5i).

15251314, 0, Downloaded from https://onlinelibrary.wiley.com/doi/10.1111/jmg.12765 by Universidad De Granada, Wiley Online Library on [11/04/2024]. See the Terms and Conditions (https://onlinelibrary.wiley.com/terms-and-conditions) on Wiley Online Library for rules of use; OA articles are governed by the applicable Creative Commons License

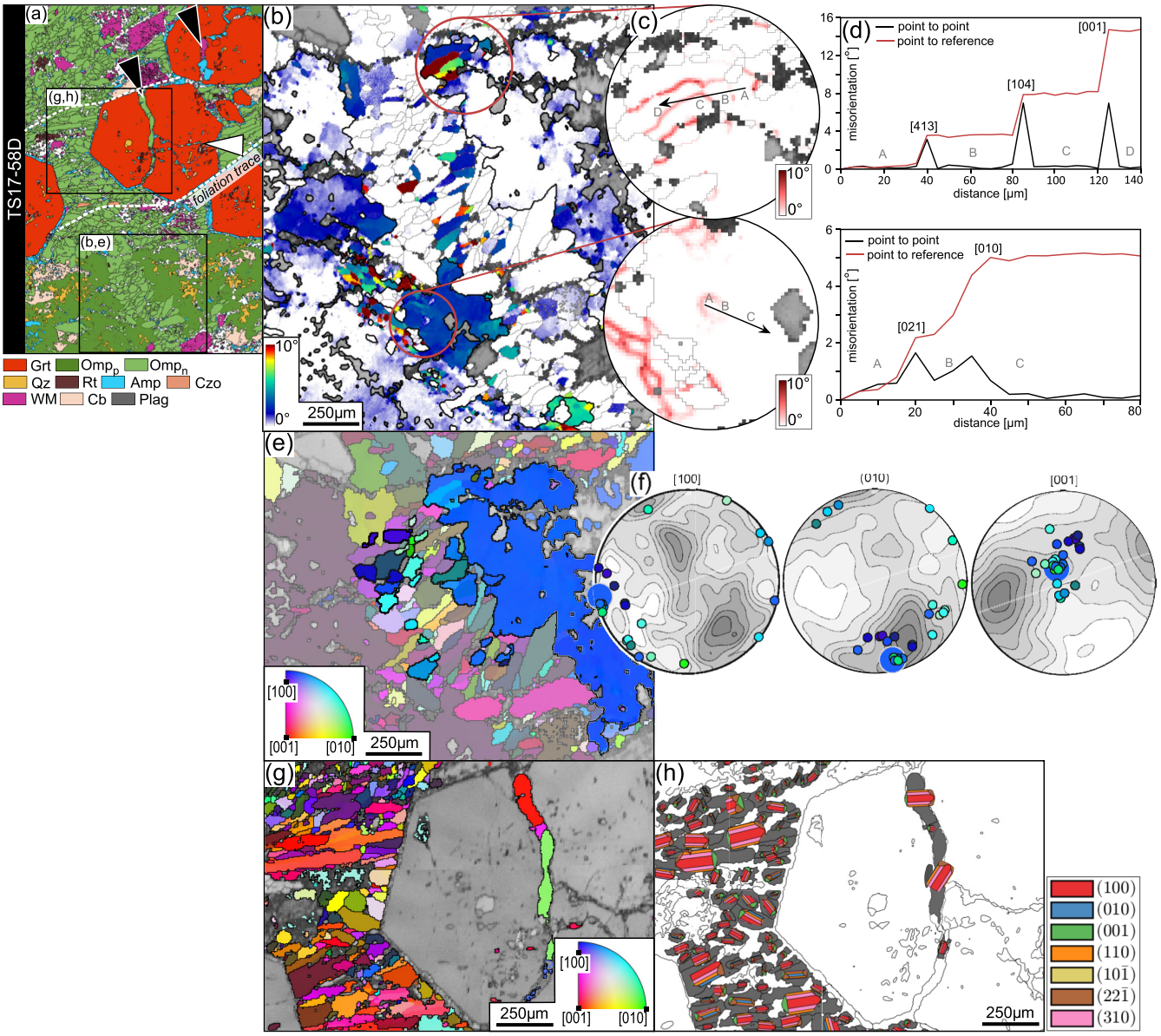


**FIGURE 7** Microstructures and intragranular lattice distortion of omphacite. (a) EBSD phase maps of selected areas from the weakly-foliated TS17–58D eclogite. Black rectangles mark the locations of close-up maps (b,e and g,h). Black triangles point to dilated microfractures in garnet ([sub]perpendicular to foliation), whereas white triangles indicate closed microfractures ([sub]parallel to foliation) (b) EBSD maps of omphacite intracrystalline misorientation (Mis2Mean). Grey colours represent the band contrast of phases other than omphacite. Mis2Mean shows higher strain in omphacite porphyroblasts and increasing misorientation towards the grain boundary, whereas the omphacite neoblasts are low-strain or strain-free. Red circles show areas presented on (c) displaying second nearest-neighbour Kernel Average Misorientation (2nd order KAM). (d) the misorientation profiles along lines marked on images (c) displaying sharp or gradual increase of misorientation and rotation axes accommodating dislocation. (e) Inverse pole figure (IPF) map showing omphacite orientation with respect to the x-vector (horizontal line). Highlighted grains form an orientation family, i.e., porphyroblasts (big circle) and surrounding neoblasts (small circles) of similar orientation. (f) Lower hemisphere, equal-area pole figures showing [100], (010) and [001] of the orientation family displaying a close grouping of [001] axis. Colouring corresponds to IPF figures. Grey contouring in the background shows CPO of omphacite neoblast in this sample – note, that the orientation of the highlighted family is discordant to the bulk omphacite CPO. (g) IPF map showing omphacite orientation in reference to the x-vector (horizontal). (h) Omphacite with superposed ideal clinopyroxene crystal shapes reflecting the crystallographic orientation of omphacite grains (exceeding 100 pixels in size). The size of crystal shape drawing is proportional to the area of the corresponding grain in the map. Note that the orientation of the [001] axis of omphacite sealing garnet microfracture is perpendicular or oblique to the fracture wall.

15251314, 0, Downloaded from https://onlinelibrary.wiley.com/doi/10.1111/jmg.12765 by Universidad De Granada, Wiley Online Library on [11/04/2024]. See the Terms and Conditions (https://onlinelibrary.wiley.com/terms-and-conditions) on Wiley Online Library for rules of use; OA articles are governed by the applicable Creative Commons License

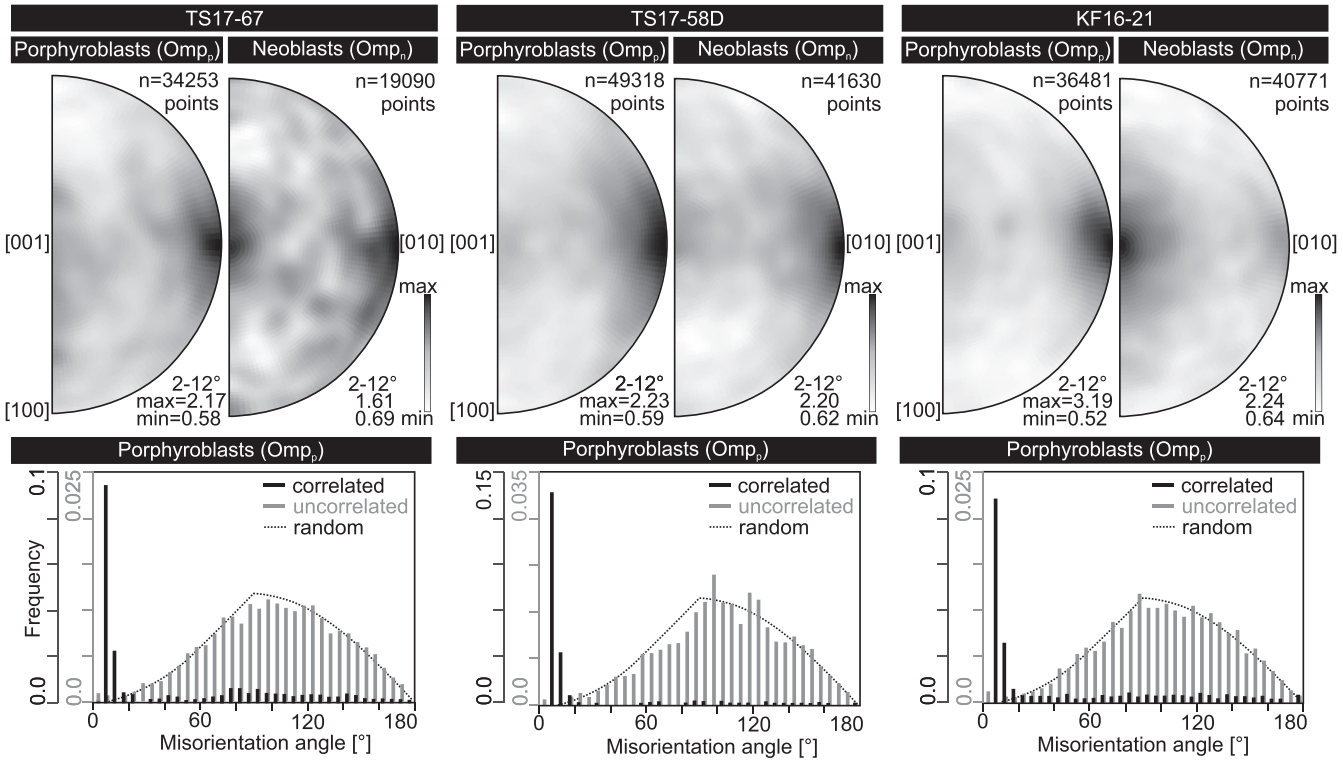


**FIGURE 8** Upper hemisphere, equal-area pole figures showing distribution of rotation axes accommodating low angle (2–12°) misorientations within omphacite porphyroblasts and neoblasts, and histograms of distribution of misorientation angles in omphacite porphyroblasts. Distribution is dominated by low-angle values for correlated pairs. Note, that the relative frequency shown along the *y*-axis of the diagram has different values for correlated and uncorrelated pairs. The theoretical random distribution corresponds to the *y*-axis scale of uncorrelated pairs.

### 4.2.5 | Rutile

Rutile occurs either within garnet or within the matrix. Grains often show exsolutions of ilmenite and are rimmed by titanite in more retrogressed domains. The matrix rutile forms single grains or clusters of several grains stretched along the foliation (Figure 5h). It shows strong to moderate SPO in Ph-bearing samples concordant to the foliation (Figure 2). Rutile in the Ph-free sample shows two orientations; one parallel and the other normal to the weak SPO of omphacite neoblasts. An observed spread distortion may originate from the thin section cut and the exposure of anisotropic grain shapes in the observed plane. Nevertheless, the rutile CPO shows the same systematic correlation to that of omphacite neoblasts in all three eclogite types. This CPO is characterized by the distribution of point-like $[001]_{Rt}$ and $[100]_{Rt}$ maxima subparallel to those of $[001]_{Omp\text{-}n}$ and $(010)_{Omp\text{-}n}$, respectively (Figure 9). Moreover, in the weakly- and moderately-foliated eclogites – samples TS17–58D and KF16–21– the maxima of $[001]_{Rt}$ and $[001]_{Omp\text{-}n}$ are distributed in the plane of the foliation subparallel to the most dominant SPO direction, and those of $[100]_{Rt}$ and $(010)_{Omp\text{-}n}$ are at the pole of the foliation (cf. Figures 2 and 9).

### 4.2.6 | Clinozoisite

Clinozoisite forms rare and small grains (<75 μm) restricted to Lws-pseudomorphs in the garnet core. Additionally, scarce clinozoisite poikiloblasts ($Czo_3$) are randomly distributed within the matrix of Ph-bearing eclogites (Figure S4). Poikiloblasts are chemically zoned, as expressed by varying $X_{Fe}^{3+}$. However, no systematic zoning pattern can be observed in the studied samples.

## 5 | P–T ESTIMATES

### 5.1 | Conventional thermobarometry

Conventional thermobarometry has been used to estimate P–T conditions of the Grt + Omp + Ph assemblage in the Ph-bearing eclogites. The method of the exchange thermometer between garnet and clinopyroxene

15251314, 0, Downloaded from https://onlinelibrary.wiley.com/doi/10.1111/jmg.12765 by Universidad De Granada, Wiley Online Library on [11/04/2024]. See the Terms and Conditions (https://onlinelibrary.wiley.com/terms-and-conditions) on Wiley Online Library for rules of use; OA articles are governed by the applicable Creative Commons License

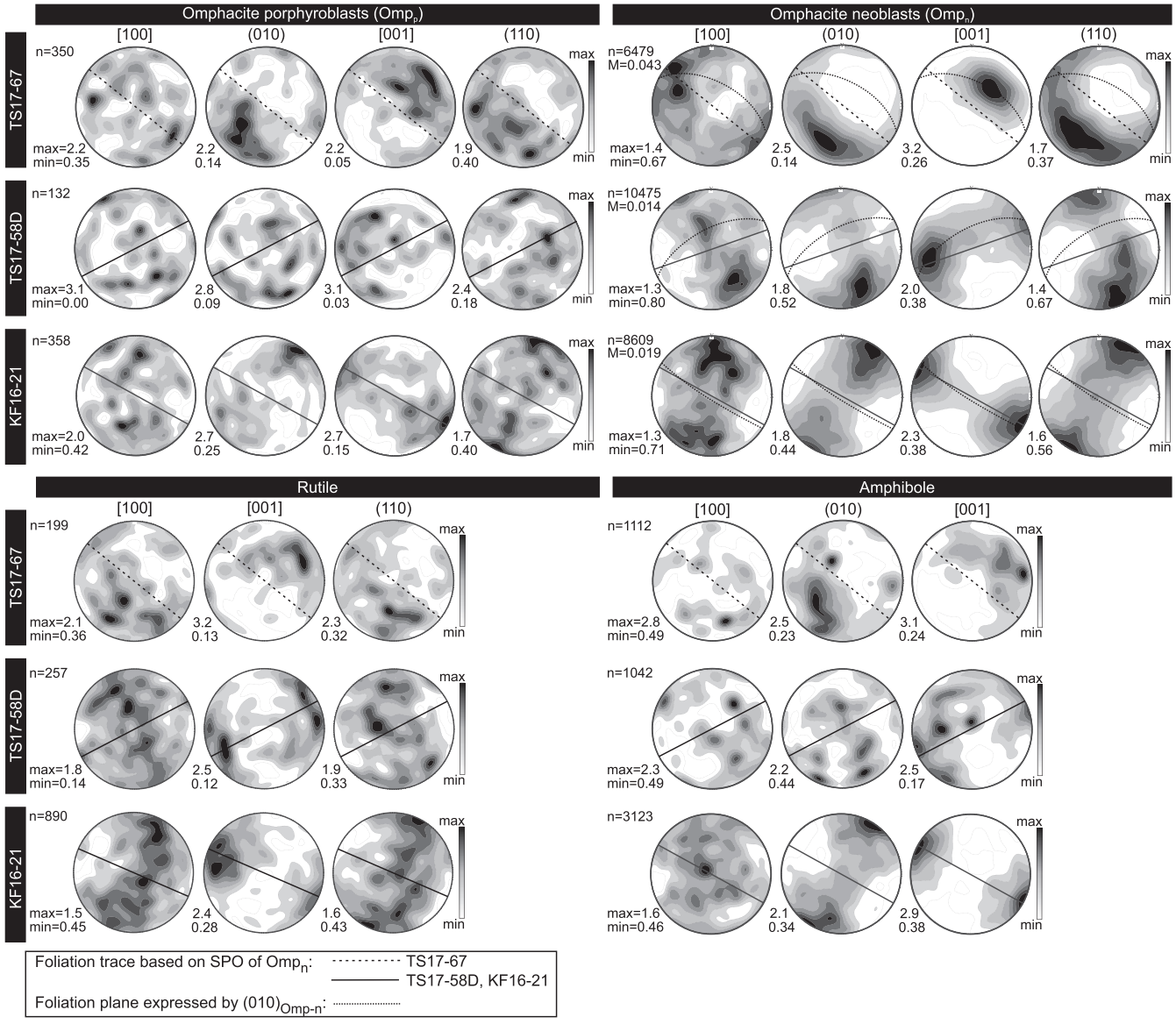


**FIGURE 9** Lower hemisphere, equal-area pole figures showing one-point-per-grain CPO of [100] and [001] axes and (010) and (110) planes of omphacite porphyroblasts ($Omp_p$), omphacite neoblasts ($Omp_n$) and amphibole. For rutile, the [100], [001] axes and (110) plane are presented. Grey colouring of scale bars is linear. Solid lines in samples KF16–21 and TS17–58D, and dashed line in TS17–67 pole figures show trace of foliation plane expressed by the SPO of omphacite neoblasts. Dashed lines on omphacite neoblasts pole figures show plane perpendicular to $(010)_{Omp\text{-}neoblast}$ indicate the foliation plane.

(Ravna, 2000) has been coupled with a barometer calibrated by Ravna and Terry (2004), based on the reaction:

$$[1]\ 6\,Di + 3\,Msc = 3\,Cel + 2\,Gro + Prp$$

The activity models of phengite (Holland & Powell, 1998), clinopyroxene (Holland, 1990) and garnet (Ganguly et al., 1996) have been used. To obtain P–T conditions of peak-P metamorphism, the chemical compositions of the outer parts of texturally correlated minerals have been used: (i) garnet rim ($Grt_2$) with the highest $(a_{grs})^2 a_{prp}$ following the protocol of Ravna and Terry (2004), (ii) phengite ($Ph_2$) in the matrix with the highest content of Si per formula unit (apfu) and (iii) omphacite ($Omp_2$) in the matrix with the highest jadeite ($X_{Jd}$) content. These calculations performed on two Ph-bearing eclogite samples yielded peak-P conditions of 2.62 GPa at 642°C (KF16–21; Figures 11 and 12) and 2.57 GPa at 667°C (TS17–58D).

## 5.2 | Zirconium-in-rutile (Zr-in-Rt) thermometry

The Zr-in-Rt thermometer has been utilized to compare with temperature estimates provided by conventional

15251314, 0, Downloaded from https://onlinelibrary.wiley.com/doi/10.1111/jmg.12765 by Universidad De Granada, Wiley Online Library on [11/04/2024]. See the Terms and Conditions (https://onlinelibrary.wiley.com/terms-and-conditions) on Wiley Online Library for rules of use; OA articles are governed by the applicable Creative Commons License

geothermometry. Rutile grains in two textural positions have been analysed: (i) rutile inclusions hosted in garnet and (ii) rutile grains in the matrix. For rutile inclusions, care was taken to only analyse grains hosted in seemingly intact garnet. However, it cannot be ruled out that some inclusions were not exposed to the matrix above and below the thin section plane. Analyses contain up to 200 μg/g of Si, which is an accepted value precluding contamination from nearby silicates (e.g., zircon inclusions; Luvizotto & Zack, 2009). The measured Fe content does not exceed 6,654 μg/g, which is below the value that might influence Zr incorporation and affect the temperature estimates (Zack et al., 2004). The Zr-in-Rt temperatures have been estimated using Kohn's (Kohn, 2020) *P*-dependent calibration based on the combined, i.e., experimental and natural data sets in the α-quartz stability field. This calibration offers improved accuracy of Zr-in-Rt thermometry (Kohn, 2020), although the calculated temperatures are up to 40°C lower for HP-LT rocks than those delivered by the Tomkins et al. (2007) calibration. In all samples, rutile grains without ilmenite exsolutions or titanite overgrowths have been preferentially analysed to avoid potential secondary Zr variations related to recrystallization.

The *P*-dependent calibration provides temperatures outlining a P–T space with a positive (dP/dT) slope (Kohn, 2020). However, for ease of comparison, temperatures for both rutile groups have been calculated at a fixed pressure of 2.5 GPa based on the conventional thermobarometry results. Usage of a lower pressure would result in obtaining a lower temperature for a given Zr concentration. The temperature estimate uncertainty is reported at the 2σ level. Rutile inclusions show systematically lower Zr concentrations with respect to matrix rutile within each sample (Table S5). In the Ph-free eclogite (TS17–67), inclusions display an average of 116 ± 43 μg/g (n = 23) and matrix grains yield 148 ± 45 μg/g (n = 18), providing 609 ± 62°C and 631 ± 53°C, respectively (Figure 10). Rutile in eclogite TS17–58D shows the lowest overall Zr concentrations with an average for rutile inclusions of 81 ± 22 μg/g (n = 12) and matrix rutiles of 97 ± 32 μg/g (n = 14). Mean temperatures do not exceed 600°C as inclusions display 583 ± 39°C and matrix rutile 596 ± 50°C. In contrast, rutile in eclogite KF16–21 shows high Zr concentrations with an average of 119 ± 32 μg/g (n = 16) for inclusions, and 179 ± 26 μg/g (n = 25) for matrix grains. Inclusions yield a broad temperature range with a mean of 614 ± 42°C, and the matrix rutile provides a concise group with a mean of 649 ± 27°C.

For all eclogites, a cumulative probability plot for rutile inclusions displays two, partially overlapping peaks at ~570 and ~610°C, while matrix rutile also shows two peaks at higher temperatures of ~610 and ~650°C (Figure 10). The individual eclogites yield different combinations of these peaks. The rutile inclusions from eclogites TS17–58D and KF16–21 display one well-pronounced peak at ~570 and ~610°C, respectively. Notably, rutile inclusions from TS17–67 display two peaks at ~570 and ~650°C. Matrix rutile show two small peaks at ~570 and ~610°C (TS17–58D) as well as ~610 and ~650°C (TS17–67). In contrast, in sample KF16–21 matrix rutile displays one peak at ~650°C.

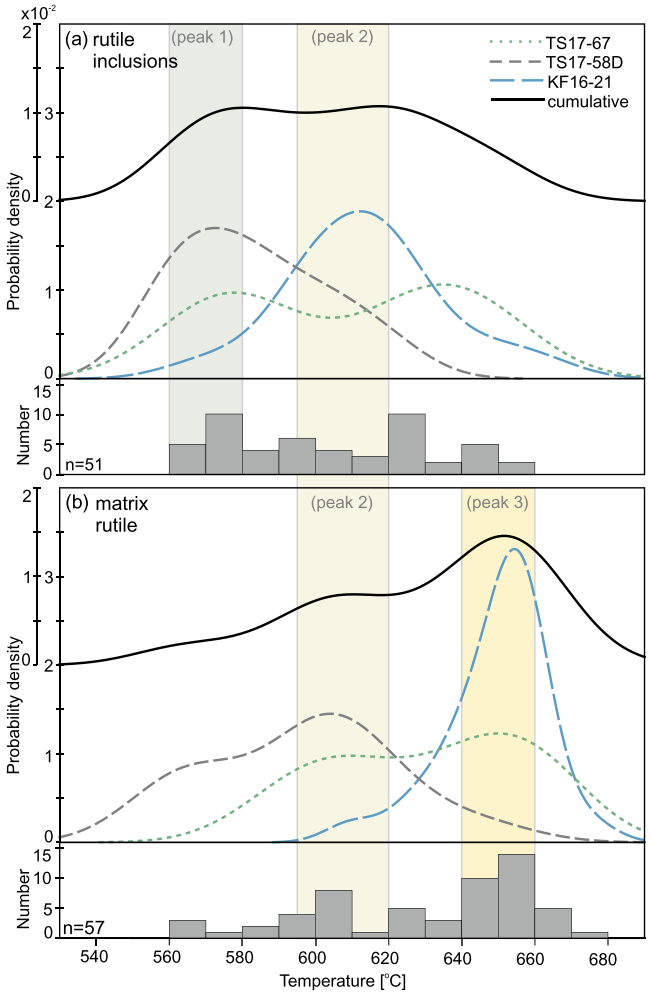


**FIGURE 10** Zr-in-rutile (Zr-in-Rt) thermometry results (°C, at fixed pressure of 2.5 GPa). (a) Results from rutile inclusions. (b) Results from matrix rutile. The inset histograms show a cumulative frequency of temperatures for the entire set of rutile inclusions (n = 51) and matrix rutile (n = 57). Dashed lines represent a kernel density estimate (KDE) of probability function derived from each sample. Solid lines represent a KDE on a cumulative dataset for rutile inclusions and matrix rutile. Colour fields represent cumulative peaks 1–3 of Zr content in both inclusions and matrix rutile grains. Note that the first *y*-axis (0.0–4.0 × $10^{-2}$) refers to the temperature probability of each sample. The second inset *y*-axis (0.0–2.0 × $10^{-2}$) refers to the temperature probability of the cumulative dataset.

15251314, 0, Downloaded from https://onlinelibrary.wiley.com/doi/10.1111/jmg.12765 by Universidad De Granada, Wiley Online Library on [11/04/2024]. See the Terms and Conditions (https://onlinelibrary.wiley.com/terms-and-conditions) on Wiley Online Library for rules of use; OA articles are governed by the applicable Creative Commons License

## 5.3 | Phase equilibrium modelling

Phase equilibrium diagrams have been constructed using Perple_X 6.7.5 software (Connolly, 1990, 2005) with the internally consistent thermodynamic database 'hp04ver' (Holland & Powell, 1998 with later updates). The phengite-bearing eclogite KF16–21 has been modelled in the 11-component system: $Na_2O$–CaO–$K_2O$–FeO–MgO–MnO–$Al_2O_3$–$SiO_2$–$H_2O$–$TiO_2$–$O_2$ (NCKFMMnASHTO), whereas the Ph-free eclogite TS17-67 has been modelled in a 10-component system: $Na_2O$–CaO–FeO–MgO–MnO–$Al_2O_3$–$SiO_2$–$H_2O$–$TiO_2$–$O_2$ (NCFMMnASHTO) due to lack of potassium in the bulk composition (Figure 11, Table S2). In both models, the following solution models have been used: garnet (White et al., 2007), clinopyroxene (Diener & Powell, 2012), white mica (Auzanneau et al., 2010), amphibole (Powell & Holland, 1999), epidote, (Holland & Powell, 1998), chlorite (Holland et al., 1998), ilmenite (White et al., 2000), biotite (White et al., 2007) and plagioclase (Newton et al., 1980). Both eclogites have been modelled in the P–T range of 1.5–3.0 GPa and 450–750°C (Figure 11). To assess the stability of Lws-bearing assemblages, all models assume pure $H_2O$ fluid saturation (e.g., Clarke et al., 2006) using a fluid equation of state by Holland and Powell (1991, 1998). Bulk compositions used for modelling come from bulk-rock analyses in wt.% that were transformed and normalized to mol.% of oxides (Table S3). The molar bulk rock $X_{Fe^{3+}} = Fe^{3+}/(Fe^{2+}+Fe^{3+})$ value of <0.05 has been used in both samples based on the satisfactory match between modelled and EBSD-derived modal composition (±3 vol.% for Grt and ±1 vol.% for Omp; Figures S5 and S6). The evolution of the mineral assemblages, density and $H_2O$ content has been calculated along a cold geotherm of 250°C/GPa (~8°C/km) in the temperature range of 500–650°C, corresponding to a pressure increase between 2.0–2.6 GPa (Figure 11c,f). This gradient has been arbitrarily chosen for modelling of the prograde path as the scarce petrographic record prevents the reconstruction of a detailed prograde P–T trajectory. Alternative prograde paths intersect the critical dehydration reactions at similar P–T values, leading to comparable results of (i) modal composition, (ii) amount of released water and (iii) densification, regardless of the slope (Figure 12).

### 5.3.1 | Phengite-free eclogite (sample TS17–67)

Within the temperature range of 450–600°C, the lawsonite/clinozoisite transition is represented by narrow fields of positive slopes placed approximately 0.2 GPa below the assumed geotherm (Figure 11a). Above 600°C, the Lws-out line becomes steeper and intersects the assumed geotherm at ~2.4 GPa and 610°C. Garnet is stable over the entire range of P–T conditions, however, its modal content is positively correlated with a decreasing amount of chlorite. At the 570–610°C interval, garnet increases by ~12 vol.%, which roughly matches the volume gained by garnets during the overgrowth of $Grt_2$ rims (cf. Figure 5a). The compositional isopleths were plotted for garnet ($Grt_2$; $X_{Grs} = 0.17–0.21$, $X_{Prp} = 0.35–0.39$, $X_{Alm} = 0.42–0.44$) and omphacite ($Omp_2$; $X_{Na} = 0.40–0.43$) (Figure 11b). The intersecting compositional isopleths constrain a narrow P–T range of 2.45–2.80 GPa and 605–650°C, encompassing stability fields of three mineral assemblages: (1) Omp + Grt + Lws + Qz + Rt, (2) Omp + Grt + Lws + Ky + Qz + Rt and (3) Omp + Grt + Ky + Qz + Rt. The latter reflects the inferred peak mineral assemblage.

Changes in mineral assemblage and mineral abundance predict progressive dehydration during three consecutive stages related to chlorite, amphibole and lawsonite breakdown (Figure 11c). Chlorite decomposition at 525–560°C releases ~2.6 wt.% of $H_2O$ that is partially retained by amphibole growing at the expense of primary clinopyroxene. Amphibole constitutes 25 vol.% at 570°C. Its breakdown within the temperature range of 570–610°C denotes the second stage of dehydration and release of ~1.0 wt.% of $H_2O$. The following lawsonite breakdown represents the third stage that leads to an abrupt release of ~1.0 wt.% of $H_2O$ at the small temperature interval of 605–615°C. Collectively, the temperature increase from 525 to 615°C results in a cumulative release of ~4.6 wt.% of $H_2O$ coupled with densification from 3.21 to 3.55 g/cm$^3$.

### 5.3.2 | Phengite-bearing eclogite (sample KF16–21)

Sample KF16–21 was chosen for modelling as it is the only sample where phengite inclusions in garnet have been found. This textural criterion attests to phengite stability during prograde stages and its presence results from the protolith bulk composition (see discussion). Even though the modelled lawsonite/clinozoisite transition is narrower, and the Lws-out line is steeper than in eclogite TS17–67 and it still intersects with the assumed prograde geotherm at the same conditions of ~2.4 GPa and 610°C (Figure 11d). The compositional isopleths were plotted for the garnet rim ($Grt_2$; $X_{Grs} = 0.21–0.24$, $X_{Prp} = 0.24–0.27$, $X_{Alm} = 0.59–0.52$) and phengite ($Ph_2$; Si = 3.31–3.39 apfu) (Figure 11e). The P-dependent Si apfu and $X_{Grs}$

15251314, 0, Downloaded from https://onlinelibrary.wiley.com/doi/10.1111/jmg.12765 by Universidad De Granada, Wiley Online Library on [11/04/2024]. See the Terms and Conditions (https://onlinelibrary.wiley.com/terms-and-conditions) on Wiley Online Library for rules of use; OA articles are governed by the applicable Creative Commons License

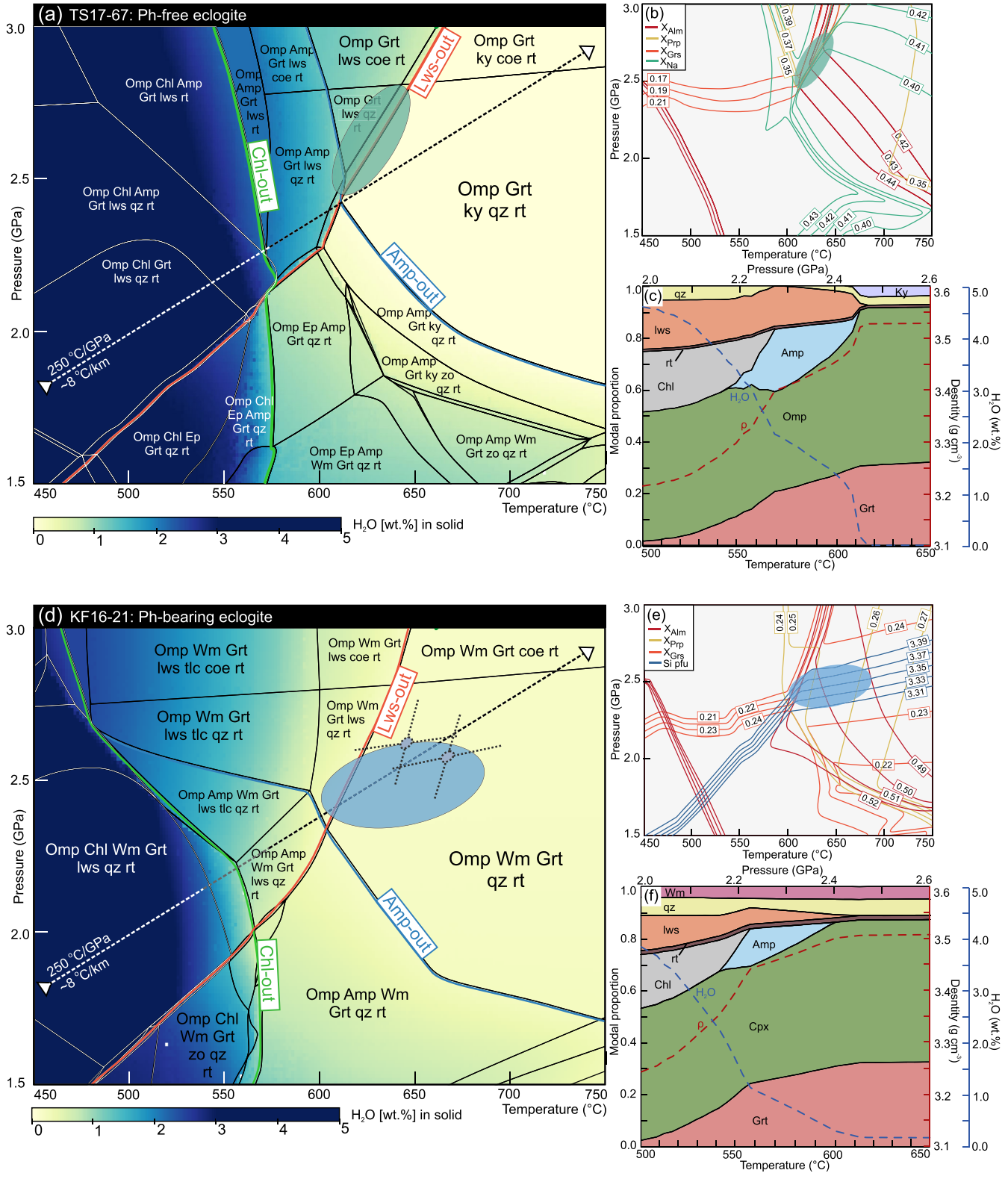


**FIGURE 11** Phase equilibrium diagrams. (a - c) diagrams of the Ph-free sample TS17–67. (d – f) diagrams of the Ph-bearing sample KF16–21. Dotted black lines on (d) show the results of Grt-Cpx thermometry (Ravna, 2000) and Cpx-Ph-Grt barometry (Ravna & Terry, 2004) in Ph-bearing samples. The colouring of (a) and (d) diagrams reflects the amount of pure $H_2O$ fluid (wt.%) remaining in mineral phases. The thick lines show out-reactions of chlorite (green), amphibole (blue) and lawsonite (orange). Isopleths in (b) and (e) show the $Grt_2$ ($X_{Alm}$, $X_{Prp}$ and $X_{Grs}$), $Omp_2$ ($X_{Na}$ in KF17–67) and $Ph_2$ (Si apfu in KF16–21) compositions. Ellipses outline the intersection of isopleths containing the peak-P conditions. Diagrams (c) and (f) show changes in mineral assemblages during subduction along the −250°C/GPa geotherm. The dashed blue line ($H_2O$) represents the amount of $H_2O$ (wt.%) left mineral phases. The dashed red line (ρ) shows changing density (g/cm$^3$) of the sample.

15251314, 0, Downloaded from https://onlinelibrary.wiley.com/doi/10.1111/jmg.12765 by Universidad De Granada, Wiley Online Library on [11/04/2024]. See the Terms and Conditions (https://onlinelibrary.wiley.com/terms-and-conditions) on Wiley Online Library for rules of use; OA articles are governed by the applicable Creative Commons License

isopleths coupled with T-dependent $X_{Alm}$ and $X_{Prp}$ constrain a P–T range of 2.30–2.55 GPa and 600–690°C. These estimates encompass fields of two mineral assemblages: (1) Omp + Ph + Grt + Lws + Qz + Rt and (2) Omp + Ph + Grt + Qz + Rt, while the latter is observed in the sample.

Changes in mineral assemblages show that dehydration of the Ph-bearing samples was progressive, but two-staged (Figure 11f). The first stage is linked to the simultaneous breakdown of chlorite and lawsonite during the 500–560°C temperature increase, releasing 2.6 wt.% of $H_2O$. Similar to the Ph-free sample, the second stage is related to amphibole and lawsonite breakdown. Within the 560–610°C temperature range, 1.2 wt.% of $H_2O$ is released. The transition from Lws-blueschist to eclogite at 500–610°C was associated with a total release of 3.8 wt.% of $H_2O$ and densification from 3.24 to 3.52 g/cm$^3$.

# 6 | DISCUSSION

## 6.1 | Metamorphic and (micro) structural evolution of Tsäkkok eclogites

### 6.1.1 | Metamorphic mineral assemblages

Three high-pressure metamorphic stages have been distinguished based on the textural relationships observed (Figure 4):

1. The M1 (prograde blueschist stage) is represented by inclusions in the garnet core and decomposed amphibole porphyroblasts in the matrix. It consists of an amphibole (Na-Ca)-$Amp_1$ (i.e., taramite, winchite and katophorite) and (Na)-$Amp_1$ (i.e., glaucophane), omphacite ($Omp_1$), garnet ($Grt_1$), rutile, quartz, lawsonite, chlorite ($Chl_1$), paragonite ($Pg_1$) ± phengite ($Ph_1$). The contacts between inclusions and garnet are sharp and it is assumed these minerals grew simultaneously. Although lawsonite has not been identified, the garnet cores host numerous Lws-pseudomorphs (for details, see Bukała et al., 2020). The Lws-pseudomorphs predominantly display a rhomboidal shape and consist of Czo ± Qz ± Ky ± $Pg_1$.
2. The M2 (peak-P/eclogite stage) includes garnet rims and their inclusions as well as the omphacite porphyroblast rims and omphacite neoblasts in the matrix. It consists of garnet ($Grt_2$), omphacite ($Omp_2$), rutile, quartz ± kyanite (in Ph-free type) ± phengite ($Ph_2$ in Ph-bearing type). Uniformly oriented omphacite neoblasts aligned with phengite ($Ph_2$), rutile and quartz define a weak to moderate foliation.
3. The M3 (post-peak-P/amphibolite stage) is represented by minerals growing at the expense of M1 and M2 assemblages. It consists of amphibole ((Na-Ca)-$Amp_3$, i.e., winchite and katophorite), quartz, paragonite ($Par_3$), diopside ($Di_3$) and clinozoisite ($Czo_3$). In the Ph-bearing samples, the omphacite porphyroblasts are often replaced by (Na-Ca)-$Amp_3$, whereas in the Ph-free samples, the breakdown to $Par_3$ ± $Di_3$ ± Qz is observed. Overall, the M3 assemblage appears to be low or strain-free and denotes post-kinematic crystallization.

The late stages of retrogression are denoted by the growth of amphibole ((Ca)-$Amp_4$, i.e., pargasite, sadanagaite and actinolite) at the expense of garnet, (Ca)-$Amp_4$ ± Pl ± Qz ± $Di_{3–4}$ symplectites after omphacite and titanite after rutile.

### 6.1.2 | Prograde to peak-P metamorphism – textural evidence

Despite the minor differences in eclogite facies assemblages and various degrees of retrograde alteration, all of the studied eclogites record similar metamorphic evolutions, expressed by both mineral chemistry and microstructures. The petrography and thermobarometric results show that all eclogites record metamorphism along a uniform, clockwise P–T path. The M1 assemblage, preserved mostly as inclusions in garnet, attests to a passage through blueschist facies from the early to late stages of prograde metamorphism. Inclusions of $Omp_1$, Lws-pseudomorphs, $Chl_1$ and (Na-Ca)-$Amp_1$and (Na)-$Amp_1$ hosted within the garnet core ($Grt_1$), suggest coeval stability during the entrapment in garnet. Although the growth of omphacite at the expense of the (Na)- and (Na-Ca)-amphibole is indicative of the blueschist to eclogite facies transition (Evans, 1990; Reinsch, 1979; Ridley & Dixon, 1984), recent experiments by Cheng and Jenkins (2021) show that partial decomposition of (Na)-amphibole can lead to the prograde (or peak) formation of (Na-Ca)-amphibole coexisting with eclogite phases.

Garnet preserves a prograde zoning expressed by decreasing $X_{Alm}$, $X_{Grs}$ and $X_{Sps}$ within the core ($Grt_1$) overgrown by high-$X_{Prp}$ rim ($Grt_2$; Figure S2). Similar garnet zoning is indicative of eclogitized metabasalts and metagabbros metamorphosed within cold subduction zones of Palaeozoic to Mesozoic age (e.g., Angiboust et al., 2012; Collet et al., 2017; Groppo & Castelli, 2010 and references therein). While the corroded (Na-Ca)-$Amp_1$, (Na)-$Amp_1$ and $Pg_1$ grains in the matrix provide textural evidence for prograde decomposition, the evidence for previous lawsonite presence is provided by

15251314, 0, Downloaded from https://onlinelibrary.wiley.com/doi/10.1111/jmg.12765 by Universidad De Granada, Wiley Online Library on [11/04/2024]. See the Terms and Conditions (https://onlinelibrary.wiley.com/terms-and-conditions) on Wiley Online Library for rules of use; OA articles are governed by the applicable Creative Commons License

rhombohedral inclusions Czo + Qz ± Ky ± $Pg_1$ representing Lws-pseudomorphs (Ballevre et al., 2003; Bukała et al., 2020; Fry & Fyfe, 1969; Philippon et al., 2013).

### 6.1.3 | Prograde to peak-P metamorphism – thermodynamic modelling

Models predict garnet stability over the entire range of modelled P–T conditions. However, it becomes volumetrically significant above ~550°C, which matches conditions of modelled omphacite and amphibole coexistence (Figure 11) and likely explains the lack of inclusions of primary igneous phases. Thermodynamic models of Ph-free and Ph-bearing eclogites predict simultaneous stability of all M1 assemblage minerals from approximately 540°C (at ~2.15 GPa) up to around 610°C (at ~2.45 GPa) along the assumed geotherm. However, it cannot be ruled out that certain M1 minerals, e.g., lawsonite and chlorite, may reflect lower temperature conditions encompassing Amp-absent fields (Figure 11). Also, the temperature extent of lawsonite stability is largely controlled by the bulk composition, including $H_2O$-saturation conditions and oxygen fugacity. Lawsonite is the major $H_2O$ carrier in HP-LT metabasites and its stability largely depends on the $H_2O$ budget (Clarke et al., 2006); thus, $H_2O$-saturation was assumed to explore the full extent of lawsonite stability for a given modelled bulk composition.

Omphacite cores ($Omp_1$) show slightly higher ferric iron compared to the rims ($Omp_2$; Figure 6b), similar to those reported from Alpine metagabbros (Groppo & Castelli, 2010; Pognante & Kienast, 1987). The elevated ferric iron content in omphacite cores ($Omp_1$; Figure 6b) might reflect higher oxygen fugacity, affecting lawsonite stability by shifting the Lws-out reaction towards higher temperatures (Groppo & Castelli, 2010). The modelling reported here assumes poorly oxidizing conditions and predicts stability of Lws-bearing assemblage up to 610°C (at ~2.45 GPa; Figure 11). Assuming a highly oxidizing environment expands the lawsonite stability up to the peak-P conditions in Ph-bearing eclogite, contradicting the observed lawsonite-absent assemblages in both modelled eclogites (Figure S6). In Ph-free eclogite, the lawsonite is predicted to break down below peak-P conditions regardless of the oxygen fugacity (Figure S5). Therefore, the elevated $X_{Fe}^{3+}$ in $Omp_1$ might be inherited from the igneous precursor (Angiboust et al., 2012), whereas $Omp_2$ reflects the overall low $X_{Fe}^{3+}$ bulk composition during prograde metamorphism that might facilitate lawsonite breakdown at relatively lower temperature of 610°C. This interpretation is also favoured due to the negligible ferric iron component in other prograde phases.

Given the scarce record of M1 assemblage and uncertainties of $X_{Fe}^{3+}$ within the lawsonite stability field at blueschist facies conditions, the exact trajectory of the prograde P–T path is uncertain (Figure 12a). Nevertheless, alternative prograde paths (shaded areas in Figure 12a) intersect the critical dehydration reactions within a similar P–T range. The modelled compositional isopleths constrain a P–T range of 2.45–2.80 GPa and 605–650°C for Ph-free, and 2.30–2.55 GPa and 600–690°C for Ph-bearing eclogite. It confirms that the M2 assemblage formation took place at conditions barely exceeding lawsonite stability fields (Figure 11a,d).

### 6.1.4 | Prograde to peak-P metamorphism – thermobarometry

Rutile inclusions in garnet show consistently lower Zr content with respect to matrix rutile, thus, record lower temperature. Due to a lack of textural evidence of recrystallization, these temperatures are interpreted as entrapment temperatures along the prograde path. Even though monophase rutile inclusions within intact garnet were preferentially analysed, a fraction of rutile inclusions might be exposed due to the common fracturing of garnet and record post-entrapment re-equilibration in sample TS17–67. Notably, using 2.5 GPa for the calculation of temperatures (see Section 5.2), these results reflect a maximum temperature estimate for prograde conditions. In contrast, matrix rutile in all samples show a wider temperature range with two peaks. The uneven distribution of Zr observed in matrix rutile within each eclogite sample may indicate (i) incomplete equilibration of prograde rutile to peak conditions (Penniston-Dorland et al., 2018), or (ii) various local equilibration conditions hindered by slow reactions at low-temperature conditions (e.g., Cheng & Jenkins, 2021). Although the current dataset does not allow us to pinpoint the exact reason for the lower Zr peaks, the higher Zr peaks contain more significant information. Considering uncertainties in prograde rutile equilibration and the bias of Zr-in-Rt towards lower temperatures (Penniston-Dorland et al., 2018), the interpretation is that higher Zr peaks represent maximum temperatures along the reconstructed P–T path. The higher Zr content peaks yield ~610°C in sample TS17–58D, and ~650°C in samples TS17–67 and KF16–21, which is in line with the thermodynamically predicted conditions (Figure 11). The conventional thermobarometry calculations, based on the chemistry of M2 minerals, pinpoint conditions of the peak-P event at 2.62 GPa and 642°C (KF16-21) and 2.57 GPa at 667°C (TS17-58D; Figure 12).

15251314, 0, Downloaded from https://onlinelibrary.wiley.com/doi/10.1111/jmg.12765 by Universidad De Granada, Wiley Online Library on [11/04/2024]. See the Terms and Conditions (https://onlinelibrary.wiley.com/terms-and-conditions) on Wiley Online Library for rules of use; OA articles are governed by the applicable Creative Commons License

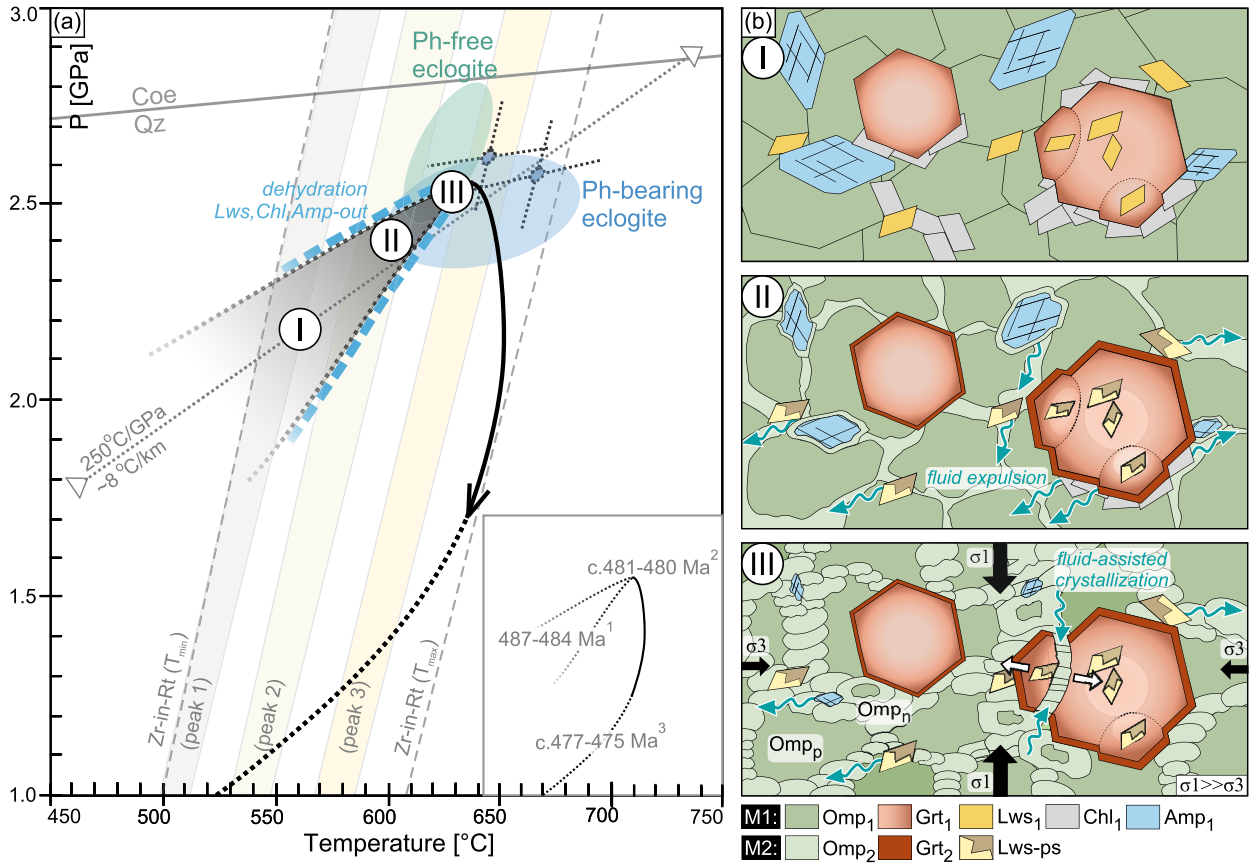


**FIGURE 12** P–T-d diagram (a) deduced pressure-temperature-deformation-time (P–T–t-d) path of Tsäkkok eclogites. Shaded area limited by dotted lines represent uncertainties regarding the prograde P–T trajectory. Dotted black lines show the results of Grt-Cpx thermometry (Ravna, 2000) and Cpx-Ph-Grt barometry (Ravna & Terry, 2004). Grey field shows the temperature range calculated for rutile inclusions and matrix rutile. Green and blue ellipses show the results of thermodynamic modelling presented in Figure 11. Ages of prograde [(1)] Fassmer et al. (2021), peak [(2)] Root and Corfu (2012), and retrograde metamorphism [(3)] Barnes et al. (2020) for the eclogite. (b) a simplified model of metamorphic and textural development during dehydration. (I) Incipient breakdown of M1 assemblage. (II) growth of M2 assemblage, and profuse fluid production. (III) further growth of M2 assemblage. Dynamic recrystallization of omphacite and brittle fracturing of garnet in response to hydrolytically induced deformation.

### 6.1.5 | Retrograde metamorphism

Replacement of omphacite by (Na-Ca)-$Amp_3$ (winchite and katophorite) suggests that the first post-eclogite stage of recrystallization started when the rocks were still in high-pressure conditions. Provided the formation of hydrous minerals at the expense of omphacite, it is inferred that the released fluid was not entirely removed from the rock volume and facilitated incipient retrograde recrystallization. The exact P–T conditions are difficult to estimate. However, an increase in $X_{Ca}$ in matrix amphibole reflects decreasing pressure (e.g., Palin et al., 2014) during the formation of the M3 assemblage. Therefore, these temperatures are interpreted to retain conditions of the eclogite facies and attest that eclogites did not experience heating during exhumation beyond the temperature of ~650°C. Altogether, this infers either isothermal decompression or cooling from peak-P conditions.

## 6.2 | Eclogite rheology

### 6.2.1 | Deformation mechanisms at the estimated P–T conditions

There is no significant difference in the deformation record between Ph-bearing and Ph-free eclogites, thus, these two groups will be collectively discussed. The cumulative Grt + Omp modal content in the studied eclogites varies from 81 to 89 vol.% and the SPO of omphacite predominantly defines the fabric. Phengite (in Ph-bearing samples), rutile and quartz show SPO in the plane of the foliation. However, the overall scarcity and relatively homogenous distribution of these minerals preclude the formation of localized high-strain bands. Therefore, the rheological behaviour of the studied eclogites can be approximated as a two-phase Grt + Omp system.

15251314, 0, Downloaded from https://onlinelibrary.wiley.com/doi/10.1111/jmg.12765 by Universidad De Granada, Wiley Online Library on [11/04/2024]. See the Terms and Conditions (https://onlinelibrary.wiley.com/terms-and-conditions) on Wiley Online Library for rules of use; OA articles are governed by the applicable Creative Commons License

Garnet in plastically deformed eclogites predominantly forms rigid grains that rarely display an SPO (e.g., Jin et al., 2001), while omphacite records more extensive deformation and formation of a strong SPO and CPO (Bascou et al., 2001; van Roermund & Boland, 1981; Zhang & Green, 2007). At the modelled peak-T conditions, exceeding 600°C, garnet can potentially deform in a ductile manner (Voegelé et al., 1999; Wang & Ji, 1999) while enhanced by the presence of fluid (Ingrin & Madon, 1995). Minor low-angle intracrystalline boundaries are attributed to the coalescence of multiple garnet cores rather than the onset of dynamic recrystallization (see Bukała et al., 2020 for further discussion). Similarly, transgranular fractures in garnet crosscut the overall prograde core-to-rim chemical zoning of garnet, and they are filled with M2 assemblage (Figure 5b,c), which is consistent with brittle behaviour of garnet at peak-P conditions. Therefore, the lack of SPO and the observed garnet microfractures attest to its predominantly brittle response to deformation at the peak-P conditions.

Omphacite rheology and deformation mechanisms at HP-LT conditions are highly debated (Zhang & Green, 2007 and references therein). The results of high-temperature (>1,000°C) deformation experiments suggest a significantly lower flow strength of jadeite and omphacite compared to diopside, questioning previously assumed strength of eclogites (Jin et al., 2001; Stöckhert & Renner, 1998). However, there is a lack of experiments at lower temperatures. Natural case studies report omphacite deformed by incipient dislocation creep at temperature >465°C (Piepenbreier & Stöckhert, 2001) with the CPO's symmetry reflecting deformation geometry, strain rates and activation of single or multiple slip systems (Helmstaedt et al., 1972; Mauler et al., 2001; Ulrich & Mainprice, 2005). The presence of omphacite porphyroblasts associated with swarms of neoblasts has been documented in naturally deformed eclogites (e.g., Mauler et al., 2001). However, it is crucial to evaluate whether this microstructure originated from brittle fracturing followed by sintering of fractured clasts or if it was formed by crystal-plastic deformation. A bimodal grain size distribution has been observed in various instances (e.g., Den Brook & Spiers, 1991). However, a lack of neoblast domains separating porphyroblasts of the same orientation (Figure 7e) precludes recrystallization along transgranular microfractures. Moreover, mineral compositions exhibit distinct concentric, prograde chemical zoning (e.g., rimward Mg enrichment in garnet and Na increase in omphacite; Figure 6), predominantly observed in garnets but often present in the omphacite porphyroblasts as well (Figure 5). These patterns show no major anisotropy or disruption, and, at the grain level, their appearance is not influenced by the structural elements of the studied eclogites (i.e., lack of resorption patterns controlled by foliation and/or lineation direction). Also, omphacite porphyroblasts show no SPO, thus, the chemically zoned mineral rims indicate crystal growth in all directions rather than substantial resorption through stress-controlled dissolution processes. Altogether, these observations imply that the textural development in the brittle regime being responsible for the omphacite microstructure can be discarded. Furthermore, it suggests that dissolution-precipitation processes likely did not play a major role in the microstructural evolution of the studied eclogites at prograde and peak-P metamorphic conditions.

To resolve mechanisms of deformation, we discuss whether the observed fabric results from dynamic or static recrystallization. Omphacite porphyroblasts have a high-strain appearance with lobate boundaries and show features of intracrystalline distortion (Figure 7b). The stacking dislocations show dominant crystallographic rotation axes of [010] and [001] (Figures 7d and 8), which along with the bulk omphacite CPO, are consistent with deformation by the combined slip system of (100)[001] and {110}1/2<110> (Bascou et al., 2001; Zhang et al., 2006). While the (100)[001] has been recognized as the easiest clinopyroxene slip system at low and intermediate temperatures, the {110}1/2<110> becomes dominant at high temperatures (Ingrin et al., 1991; Raterron et al., 1994) beyond those estimated for Tsäkkok eclogites.

Neoblasts are not entirely strain-free but exhibit minor intracrystalline deformation (Figure S3), expected for grains formed via subgrain rotation within strained porphyroblasts (Urai et al., 1986). In all samples, the CPO of neoblasts is also texturally controlled, as the orientation of some neoblasts relates to the nearby porphyroblast (Figure 7e,f). In such instances, neoblasts and porphyroblasts form orientation families with common CPO that is expressed by a concise group of [001] and more random [100] and (010), suggesting that neoblast CPO was inherited from their porphyroblast precursors. Noteworthy, the CPO of such porphyroblast-neoblast pairs are discordant to the bulk omphacite CPO. Altogether, the non-random CPO of omphacite, the non-random crystallographic axes accommodating its lattice distortions at the subgrain level, and the microstructural record of dynamic recrystallization processes are interpreted to be predominantly formed by dislocation creep deformation in these eclogites. Nevertheless, we cannot rule out that the omphacite CPO and the anisotropic crystal shapes along [001], which is considered as the fastest growth direction in clinopyroxene (e.g., van Panhuys-Sigler & Hartman, 1981), are locally also enhanced by grain growth (e.g., Figure 7g,h).

15251314, 0, Downloaded from https://onlinelibrary.wiley.com/doi/10.1111/jmg.12765 by Universidad De Granada, Wiley Online Library on [11/04/2024]. See the Terms and Conditions (https://onlinelibrary.wiley.com/terms-and-conditions) on Wiley Online Library for rules of use; OA articles are governed by the applicable Creative Commons License

### 6.2.2 | Linking metamorphism and deformation: P–T-d path

Assigning a relative timeframe for the deformation is necessary to establish a link between microstructures and metamorphic evolution and explore the potential coupling between dehydration and deformation. The observed rock fabric results from brittle deformation of garnet and ductile deformation of omphacite by dislocation creep. The transitional chemical character of the neoblasts, with zoning similar to porphyroblasts, suggests that deformation either preceded or acted simultaneously with the formation of omphacite chemical zoning (Figure 5 and stage II in Figure 12b). These microstructures, therefore, indicate a clear link between deformation and the growth of Omp ± Grt, providing constraints on the timing of deformation (prograde or peak-P conditions with M1 and M2 assemblages). It can be inferred that deformation and mineral growth occurred at the estimated HP conditions of fracturing and vein opening in some Tsäkkok eclogites (Bukała et al., 2020). Altogether, the textural relationships, microstructures and SPO of the minerals of the peak-P (M2 assemblage; Figure 4), coupled with thermobarometry results, suggest synkinematic formation during near peak-P conditions of ongoing subduction. Therefore, the omphacite CPO reflects deformation approximately coincident with the event of profuse dehydration predicted by thermodynamic modelling. The weak amphibole [001] maximum parallel to the omphacite [001] is interpreted as inheritance by amphibole during the replacement of omphacite, based on the textural relationships, similar to the observations of Rehman et al. (2023).

## 6.3 | Dehydration-driven deformation

### 6.3.1 | Dehydration and fluid source

;Thermodynamic models predict that the samples contained ∼4.0–4.6 wt.% of structurally bonded water at the onset of the dehydration (Figure 11), which is a reasonable value for hydrated metabasites (Schmidt & Poli, 1998). Within the range of ∼515–615°C, eclogites experienced either a three-stage (TS17–67) or a two-stage (KF16–21) dehydration along the assumed geotherm (Figure 11). A significant release of water was related to a cumulative breakdown of chlorite, amphibole and lawsonite that is in line with critical dehydration processes recognized in natural case studies (Groppo & Castelli, 2010; Lü et al., 2009) and in experiments (e.g., Poli & Schmidt, 1995).

A result of complete dehydration is the Ph-free eclogite type preserving the anhydrous eclogite facies assemblage of Grt + Omp + Rt + Ky + Qz. It matches the results of experiments investigating lawsonite stability suggesting that lawsonite breakdown at a pressure above zoisite stability leads to the formation of the anhydrous assemblage of Grt + Cpx + Qz/Coe ± Ky (Okamoto & Maruyama, 1999; Poli & Schmidt, 1995). Preservation of such assemblage brings forth the hypothesis that the Ph-free eclogites record in-situ dehydration and no interaction with external fluids. The more common Ph-bearing eclogites record dehydration as well, but also evidence for the stability of phengite at (near-)peak-P conditions. The abundance of phengite in a HP assemblage could result from a protolith enriched in LILE due to seafloor alteration (e.g., Angiboust & Agard, 2010) or HP fluid infiltration from external reservoir (Rubatto & Angiboust, 2015). While the phengite inclusions attest to its presence during prograde metamorphism (hence, supporting seafloor alteration), phengite infilling garnet microfractures suggest that post-fracturing crystallization was assisted by LILE-bearing fluid, either produced internally by the Ph-bearing eclogite or derived from an external source. Regardless of the underlying cause, phengite seems to reflect a fluid–rock interaction that modified the Ph-bearing, and not the Ph-free eclogites.

Noteworthy, irrespective of whether phengite is present or absent, both eclogite types record the same dehydration stages. The presence of phengite only accounts for a maximum of ∼0.5 wt.% of $H_2O$ retention, and it is not as critical for dehydration as modelled Lws-, Amp- and Chl-out reactions, which control the majority of $H_2O$ budget. The development of similar textures in both the Ph-free and Ph-bearing eclogites suggests that the presence of *internally* produced fluid likely facilitated deformation.

### 6.3.2 | Rheological effect of dehydration

Numerical modelling of simple shear of HP-LT eclogites predicts the coexistence of brittle garnet and ductile omphacite, depending on garnet volume percentage (Yamato et al., 2019) when the shear stress is generated as a consequence of densification. Even though the studied eclogites show similar microstructures to those reported by Yamato et al. (2019), the lack of porphyroblast rotation and the detailed microstructural analysis of SPO and CPO point to a negligible simple shear component during deformation. The intermediate LS indices of the omphacite can be consistent with either simple shear or pure shear deformation (Ulrich & Mainprice, 2005). However, the (i) symmetry of omphacite CPO with [001] aligned along SPO, as well as (ii) the lack of obliquity between CPO and the X structural direction, advocate

15251314, 0, Downloaded from https://onlinelibrary.wiley.com/doi/10.1111/jmg.12765 by Universidad De Granada, Wiley Online Library on [11/04/2024]. See the Terms and Conditions (https://onlinelibrary.wiley.com/terms-and-conditions) on Wiley Online Library for rules of use; OA articles are governed by the applicable Creative Commons License

against simple shear (Bouchez et al., 1983; Mainprice & Nicolas, 1989). Also, neither the 2D reconstruction of all garnet grains (Figure 2) nor the 3D modelling of single grains (Bukała et al., 2020) show any displacement between separated fragments, suggesting the lack of a significant simple shear component acting on the rocks during the opening of fractures.

Garnets amalgamated during their growth and formed arrays of coalescence planes (Bukała et al., 2020), currently displaying random orientation in each sample. These coalescence planes represent inherently weakened domains within the individual crystals and were successively exploited during garnet fracturing. However, the orientation of open-microfractures through garnets is systematically perpendicular or at a high angle (>50°) to the foliation (Figure 2). The considerable dispersion in the orientation of open-microfractures sealed by omphacite could indicate either (i) a hydrofracturing origin of these microfractures, resulting in larger spread of orientation, or (ii) tensile fracturing leading to preferential opening of certain coalescence planes aligned with the stress field (subparallel to $\sigma_1$ principal stress axis, i.e., perpendicular to the foliation). Hence, microfractures oriented subparallel to the foliation plane, thus, perpendicular to the inferred $\sigma_1$ principal stress axis remain closed (Figure 2). This observation reinforces that pure shear dominated the deformation of eclogites close to the peak-P metamorphic conditions. The microfractures are thus extensional joints, with some of them representing hybrid joints. Despite that we interpret the opening of microfractures in the studied garnets (characteristic examples highlighted by black arrows in Figure 2) as extensional joints controlled by coaxial pure shear deformation, based on the current microstructural data, we cannot exclude that some actually opened due to hydrofracturing too, similar to the conclusion reached by Bukała et al., 2020. In fact, both processes could coexist in the studied eclogites and might mutually lead to the formation of current garnet microstructures.

Altogether, based on omphacite microstructures (Figure S4), as well as the characteristic alignment of their SPO and CPO (Figures 2 and 9), the interpretation of coaxial pure shear as a dominant deformation regime is more favourable. The hydrofracturing and/or tensile fracturing of garnet coupled with rheological weakening and dynamic recrystallization of omphacite in the presence of fluid are interpreted as the dominant processes.

If the deformation and brittle fracturing of eclogite took place due to HP fluids, they may also enhance the sealing of fractures and foster recovery while the rock remained in the brittle/ductile regime (stage III in Figure 12b). Omphacite crystallization in the newly formed microfractures of garnet is expected to be fast to seal relatively large volumes without any displacement along the fractures. The orientations of such omphacite show a crystallographic relationship with the [001] axis perpendicular or slightly oblique to the fracture walls, i.e., parallel to microfracture propagation direction (Figure 7g,h). It is consistent with the expected geometries for crystal growth in veins (Bons et al., 2012), nucleated on the wall and growing towards the pore interior. Also, the fluid-assisted crystallization of omphacite accompanied by solution transfer, has been identified as an efficient mechanism for omphacite recrystallization in eclogites that record HP-LT conditions, particularly when solid-state diffusion in the absence of fluids is negligible (Stünitz et al., 2020). Thus, the fastest growth direction of the studied omphacite appears to be along the [001] (the c-axis), which denotes the smallest spacing in the crystalline structure (Cameron et al., 1973; Stünitz et al., 2020). Therefore, the orientation of garnet microfractures and CPO of omphacite within advocate for fluid-assisted, oriented crystallization of strain-free omphacite during the fracturing event.

### 6.3.3 | Tectonic remarks

The processes of fluid buildup and discharge -particularly associated with eclogitization- have been linked to intermediate-depth seismicity (Hacker et al., 2003) or episodic tremor and slip events (Behr et al., 2018). A whole rock brittle failure at eclogite-facies conditions is manifested by natural and experimentally produced pseudotachylytes, cataclasites and eclogite breccias and potentially represents the locus of earthquakes (Austrheim & Boundy, 1994; Hertgen et al., 2017; John & Schenk, 2006; Scambelluri et al., 2017; Yang et al., 2014). However, recent studies show that large-scale slip and localized shear zones are not necessary for seismometamorphic processes. The scales of microstructures linked with seismic processes vary from nanoscale- (Petley-Ragan et al., 2020), to microscale (Broadwell et al., 2019) and mesoscale (Jamtveit et al., 2018). In addition, the (micro) structures of oscillatory garnet major elements (Viete et al., 2018) and isotopic zoning (Hoover et al., 2022), off-fault fracturing/healing cycles of garnet (Broadwell et al., 2019) and tensile fracturing (Ujiie et al., 2018) have all been considered as valid manifestations of seismometamorphism.

The direct link between the Tsäkkok eclogites and deep seismicity is rather speculative since the observations lack unequivocal evidence for slip at the micro- and macro-scale. Nevertheless, the provided evidence shows that in-situ dehydration has led directly to microfracturing of eclogites at HP conditions. Unlike other studies

15251314, 0, Downloaded from https://onlinelibrary.wiley.com/doi/10.1111/jmg.12765 by Universidad De Granada, Wiley Online Library on [11/04/2024]. See the Terms and Conditions (https://onlinelibrary.wiley.com/terms-and-conditions) on Wiley Online Library for rules of use; OA articles are governed by the applicable Creative Commons License

(e.g., Angiboust et al., 2012; Rubatto & Angiboust, 2015) the Ph-free Tsäkkok eclogites show that no external fluid was necessary to trigger the brittle response. Each eclogite dehydrates at the single-crystal scale, and only when internally produced fluids collectively exceeded a volume that allowed them to propagate through eclogite, the network of brittle fractures/veins could be formed (Connolly, 2010; Miller et al., 2003; Zhang & Green, 2007). These fractures/veins correspond to the garnet- and omphacite-filled mesofractures reported by Bukała et al. (2020).

The progressive fluid buildup and discharge within the studied eclogites can be inferred from thermodynamic modelling (this study) and the chemical zoning of garnetite veins (Bukała et al., 2020). The microstructural record of the mechanical weakening by released fluids attests to a relationship between prograde dehydration and deformation in both active and fossil subduction zones. Nevertheless, heterogeneously dehydrating slabs and associated rheological changes during internal fluid production events may also substantially impact seismicity at intermediate depths of subduction zones (e.g. Ferrand et al., 2017). These processes may cause transient weakening in otherwise brittle assemblages, which then diversely respond to stresses within short timespans.

## 7 | CONCLUSIONS

Tsäkkok eclogites record prograde metamorphism through the lawsonite-blueschist to the eclogite facies. Despite the range of observed eclogite-facies mineral assemblages, all samples collectively point at ~2.5 GPa and ~620°C for eclogite facies equilibration conditions, denoting the peak-P stage along the P–T path. Prograde decomposition of chlorite, lawsonite and amphibole led to progressive dehydration and release of up to 4.6 wt.% of the *internally* produced fluid. Fluid discharge led to rheological weakening, which promoted ductile-brittle deformation. No external fluid source nor channelized fluid flow is required to facilitate a ductile-brittle deformation of eclogite in a subduction setting.

## ACKNOWLEDGMENTS

We acknowledge the constructive criticism of Luca Menegon and an anonymous reviewer, as well as the careful editorial work and comments of Johann Diener, which substantially improved the scientific content of the manuscript. This research was funded by the National Science Centre (Poland) research projects no. 2019/33/N/ST10/01479 (M. Bukała) and 2014/14/ST10/00321 (J. Majka). M.Bukała acknowledges "Juan de la Cierva" Fellowship no. JFJC2021-047505-I funded by MCIN/AEI/10.13039/501100011033, CSIC and EU Next-Generation EU/PRTR, as well as support by Foundation for Polish Science (FNP). The Agencia Estatal de Investigacion (MCIN/AEI/10.13039/501100011033) is also acknowledged by M.Bukała for funding under RUSTED project PID2022-136471N-B-C21&C22, and by K.Hidas for grant no. PID2020-119651RB-I00. We acknowledge support of the publication fee by the CSIC Open Access Publication Support Initiative through its Unit of Information Resources for Research (URICI). A. Włodek is thanked for his technical and analytical assistance during EMP analyses at AGH-UST, and L. Tual for help during fieldwork.

## ORCID

*Michał Bukała* https://orcid.org/0000-0001-7045-3150
*Károly Hidas* https://orcid.org/0000-0003-1371-0362
*Iwona Klonowska* https://orcid.org/0000-0001-7346-1770
*Christopher J. Barnes* https://orcid.org/0000-0003-0597-7999
*Jarosław Majka* https://orcid.org/0000-0002-6792-6866

## REFERENCES

Andréasson, P.-G. (1987). Early evolution of the late Proterozoic Baltoscandian margin: Inferences from rift magmatism. *Geologiska Föreningen I Stockholm Förhandlingar*, *109*(4), 336–340. https://doi.org/10.1080/11035898709453101

Andréasson, P.-G., Gee, D. G., & Sukotji, S. (1985). Seve eclogites in the Norrbotten Caledonides, Sweden. In D. G. Gee & B. A. Sturt (Eds.), *The Caledonide Orogen - Scandinavia and related areas1* (pp. 887–902). John Wiley & Sons.

Angiboust, S., & Agard, P. (2010). Initial water budget: The key to detaching large volumes of eclogitized oceanic crust along the subduction channel? *Lithos*, *120*(3–4), 453–474. https://doi.org/10.1016/j.lithos.2010.09.007

Angiboust, S., Agard, P., Yamato, P., & Raimbourg, H. (2012). Eclogite breccias in a subducted ophiolite: A record of intermediate earthquakes. *Geology*, *40*(8), 707–710. https://doi.org/10.1130/G32925.1

Arcay, D., Tric, E., & Doin, M.-P. (2005). Numerical simulations of subduction zones. *Physics of the Earth and Planetary Interiors*, *149*(1–2), 133–153. https://doi.org/10.1016/j.pepi.2004.08.020

Austrheim, H., & Boundy, T. M. (1994). Pseudotachylytes generated during seismic faulting and eclogitization of the deep crust. *Science*, *265*(5168), 82–83. https://doi.org/10.1126/science.265.5168.82

Auzanneau, E., Schmidt, M. W., Vielzeuf, D., & D'Connolly, J. A. (2010). Titanium in phengite: A geobarometer for high temperature eclogites. *Contributions to Mineralogy and Petrology*, *159*(1), 1–24. https://doi.org/10.1007/s00410-009-0412-7

Bachmann, F., Hielscher, R., & Schaeben, H. (2010). Texture analysis with MTEX – Free and open source software toolbox. *Solid State Phenomena*, *160*, 63–68. https://doi.org/10.4028/www.scientific.net/SSP.160.63

15251314, 0, Downloaded from https://onlinelibrary.wiley.com/doi/10.1111/jmg.12765 by Universidad De Granada, Wiley Online Library on [11/04/2024]. See the Terms and Conditions (https://onlinelibrary.wiley.com/terms-and-conditions) on Wiley Online Library for rules of use; OA articles are governed by the applicable Creative Commons License

Ballevre, M., Pitra, P., & Bohn, M. (2003). Lawsonite growth in the epidote blueschists from the Ile de Groix (Armorican massif, France): A potential geobarometer. *Journal of Metamorphic Geology*, *21*(7), 723–735. https://doi.org/10.1046/j.1525-1314.2003.00474.x

Barnes, C. J., Jeanneret, P., Kullerud, K., Majka, J., Schneider, D. A., Bukała, M., & Klonowska, I. (2020). Exhumation of the high-pressure Tsäkkok lens, Swedish Caledonides: Insights from the structural and White mica $^{40}$ Ar/$^{39}$ Ar geochronological record. *Tectonics*, *39*(7), e2020TC006242. https://doi.org/10.1029/2020TC006242

Barnes, C. J., Majka, J., Bukała, M., Nääs, E., & Rousku, S. (2021). Detrital zircon U-Pb geochronology of a metasomatic calc-silicate in the Tsäkkok lens, Scandinavian Caledonides. *Geology, Geophysics and Environment*, *47*(1), 21–31. https://doi.org/10.7494/geol.2021.47.1.21

Barnes, C. J., Majka, J., Jeanneret, P., Ziemniak, G., Kooijman, E., Kośmińska, K., Kielman-Schmitt, M., & Schneider, D. A. (2021). Using Th-U-Pb geochronology to extract crystallization ages of Paleozoic metamorphic monazite contaminated by initial Pb. *Chemical Geology*, *582*, 120450. https://doi.org/10.1016/j.chemgeo.2021.120450

Bascou, J., Barruol, G., Vauchez, A., Mainprice, D., & Egydio-Silva, M. (2001). EBSD-measured lattice-preferred orientations and seismic properties of eclogites. *Tectonophysics*, *342*(1–2), 61–80. https://doi.org/10.1016/S0040-1951(01)00156-1

Behr, W. M., Kotowski, A. J., & Ashley, K. T. (2018). Dehydration-induced rheological heterogeneity and the deep tremor source in warm subduction zones. *Geology*, *46*(5), 475–478. https://doi.org/10.1130/G40105.1

Boland, J. N., & Tullis, T. E. (1986). Deformation behavior of wet and dry clinopyroxenite in the brittle to ductile transition region. In B. E. Hobbs, & H. C. Heard (Eds.), *Mineral and rock deformation: Laboratory studies* (pp. 35–49). American Geophysical Union. https://doi.org/10.1029/GM036

Bons, P. D., Elburg, M. A., & Gomez-Rivas, E. (2012). A review of the formation of tectonic veins and their microstructures. *Journal of Structural Geology*, *43*, 33–62. https://doi.org/10.1016/j.jsg.2012.07.005

Bouchez, J. L., Lister, G. S., & Nicolas, A. (1983). Fabric asymmetry and shear sense in movement zones. *Geologische Rundschau*, *72*(2), 401–419. https://doi.org/10.1007/BF01822075

Broadwell, K. S., Locatelli, M., Verlaguet, A., Agard, P., & Caddick, M. J. (2019). Transient and periodic brittle deformation of eclogites during intermediate-depth subduction. *Earth and Planetary Science Letters*, *521*, 91–102. https://doi.org/10.1016/j.epsl.2019.06.008

Bukała, M., Barnes, C., Jeanneret, P., Hidas, K., Mazur, S., Almqvist, B. S. G., Kośmińska, K., Klonowska, I., Šurka, J., & Majka, J. (2020). Brittle deformation during eclogitization of early Paleozoic blueschist. *Frontiers in Earth Science*, *8*, *1–17*. https://doi.org/10.3389/feart.2020.594453

Cameron, M., Sueno, S., & Papike, J. J. (1973). High-temperature crystal chemistry of Acmite, Diopside, Hedenbergite jadeite, Spodumene and Ureyite. *American Mineralogist*, *58*(7–8), 594–618.

Cheng, N., & Jenkins, D. M. (2021). Experimental study of metamorphic reactions and dehydration processes at the blueschist–eclogite transition during warm subduction. *Journal of Metamorphic Geology*, *39*(1), 39–56. https://doi.org/10.1111/jmg.12560

Clarke, G. L., Powell, R., & Fitzherbert, J. A. (2006). The lawsonite paradox: A comparison of field evidence and mineral equilibria modelling. *Journal of Metamorphic Geology*, *24*(8), 715–725. https://doi.org/10.1111/j.1525-1314.2006.00664.x

Collet, T., Štípská, P., Kusbach, V., Schulmann, K., & Marciniak, G. (2017). Dynamics of Saxothuringian subduction channel constrained by phase - equilibia.pdf. *Journal of Metamorphic Geology*, *35*, 253–280. https://doi.org/10.1111/jmg.12226

Connolly, J. A. D. (1990). Multivariable phase diagrams: An algorithm based on generalized thermodynamics. *American Journal of Science*, *290*, 666–718. https://doi.org/10.2475/ajs.290.6.666

Connolly, J. A. D. (2005). Computation of phase-equilibria by linear programming: A tool for geodynamic modeling and its application to subduction zone decarbonation. *Earth and Planetary Science Letters*, *236*, 524–541. https://doi.org/10.1016/j.epsl.2005.04.033

Connolly, J. A. D. (2010). The mechanics of metamorphic fluid expulsion. *Elements*, *6*(3), 165–172. https://doi.org/10.2113/gselements.6.3.165

Corfu, F., Andersen, T. B., & Gasser, D. (2014). The Scandinavian Caledonides: Main features, conceptual advances, and critical questions. In F. Corfu D. Gasser D. M. Chew *New perspectives on the caledonides of Scandinavia and related areas* (pp. 9–43). London: Geological Society, Special Publications.

Den Brook, S. W. J., & Spiers, C. J. (1991). Experimental evidence for water weakening of quartzite by microcracking plus solution-precipitation creep. *Journal of the Geological Society, London*, *148*, 541–548. https://doi.org/10.1144/gsjgs.148.3.0541

Diener, J. F. A., & Powell, R. (2012). Revised activity-composition models for clinopyroxene and amphibole. *Journal of Metamorphic Geology*, *30*(2), 131–142. https://doi.org/10.1111/j.1525-1314.2011.00959.x

Droop, G. T. R. (1987). A general equation for estimating Fe $^{3+}$ concentrations in ferromagnesian silicates and oxides from microprobe analyses, using stoichiometric criteria. *Mineralogical Magazine*, *51*(361), 431–435. https://doi.org/10.1180/minmag.1987.051.361.10

Evans, B. W. (1990). Phase relations of epidote-blueschists. *Lithos*, *25*(1–3), 3–23. https://doi.org/10.1016/0024-4937(90)90003-J

Fassmer, K., Froitzheim, N., Janák, M., Strohmeyer, M., Bukała, M., Lagos, M., & Münker, C. (2021). Diachronous collision in the Seve nappe complex: Evidence from Lu–Hf geochronology of eclogites (Norrbotten, North Sweden). *Journal of Metamorphic Geology*, *39*(7), 819–842. https://doi.org/10.1111/jmg.12591

Ferrand, T. P., Hilairet, N., Incel, S., Deldicque, D., Labrousse, L., Gasc, J., Renner, J., Wang, Y., Green, H. W., & Schubnel, A. (2017). Dehydration-driven stress transfer triggers intermediate-depth earthquakes. *Nature Communications*, *8*, 15247. https://doi.org/10.1038/ncomms15247

Fry, N., & Fyfe, W. S. (1969). Eclogites and water pressure. *Contributions to Mineralogy and Petrology*, *24*(1), 1–6. https://doi.org/10.1007/BF00398749

Ganguly, J., Cheng, W., & Tirone, M. (1996). Thermodynamics of aluminosilicate garnet solid solution: New experimental data, an optimized model, and thermometric applications. *Contributions*

15251314, 0, Downloaded from https://onlinelibrary.wiley.com/doi/10.1111/jmg.12765 by Universidad De Granada, Wiley Online Library on [11/04/2024]. See the Terms and Conditions (https://onlinelibrary.wiley.com/terms-and-conditions) on Wiley Online Library for rules of use; OA articles are governed by the applicable Creative Commons License

*to Mineralogy and Petrology*, *126*(1–2), 137–151. https://doi.org/10.1007/s004100050240

Gee, D. G., Janák, M., Majka, J., Robinson, P., & van Roermund, H. (2013). Subduction along and within the Baltoscandian margin during closing of the Iapetus Ocean and Baltica-Laurentia collision. *Lithosphere*, *5*(2), 169–178. https://doi.org/10.1130/L220.1

Groppo, C., & Castelli, D. (2010). Prograde P–T evolution of a Lawsonite Eclogite from the Monviso meta-ophiolite (Western Alps): Dehydration and redox reactions during subduction of oceanic FeTi-oxide gabbro. *Journal of Petrology*, *51*(12), 2489–2514. https://doi.org/10.1093/petrology/egq065

Hacker, B. R., Peacock, S. M., Abers, G. A., & Holloway, S. D. (2003). Subduction factory 2. Are intermediate-depth earthquakes in subducting slabs linked to metamorphic dehydration reactions? *Journal of Geophysical Research*, *108*(B1), 1–16. https://doi.org/10.1029/2001JB001129

Hawkesworth, C. J., Gallagher, K., Hergt, J. M., & McDermott, F. (1993). Mantle and slab contributions in ARC magmas. *Annual Review of Earth and Planetary Sciences*, *21*(1), 175–204. https://doi.org/10.1146/annurev.ea.21.050193.001135

Hawthorne, F. C., Oberti, R., Harlow, G. E., Maresch, W. V., Martin, R. F., Schumacher, J. C., & Welch, M. D. (2012). Nomenclature of the amphibole supergroup. *American Mineralogist*, *97*(11–12), 2031–2048. https://doi.org/10.2138/am.2012.4276

Helmstaedt, H., Anderson, D. L., & Gavasci, A. T. (1972). Petrofabric studies of eclogite, spinel websterite, and spinellherzolite xenoliths from kimberlite-breccia pipes in southeastern Utah and northeastern Arizona. *Journal of Geophysical Research*, *77*, 4350–4365. https://doi.org/10.1029/JB077i023p04350

Hertgen, S., Yamato, P., Morales, L. F. G., & Angiboust, S. (2017). Evidence for brittle deformation events at eclogite-facies P-T conditions (example of the Mt. Emilius klippe, Western Alps). *Tectonophysics*, *706–707*, 1–13. https://doi.org/10.1016/j.tecto.2017.03.028

Hielscher, R., & Schaeben, H. (2008). A novel pole figure inversion method: Specification of the MTEX algorithm. *Journal of Applied Crystallography*, *41*(6), 1024–1037. https://doi.org/10.1107/S0021889808030112

Holland, T., Baker, J., & Powell, R. (1998). Mixing properties and activity-composition relationships of chlorites in the system MgO-FeO-Al2O3-SiO2-H2O. *European Journal of Mineralogy*, *10*(3), 395–406. https://doi.org/10.1127/ejm/10/3/0395

Holland, T., & Powell, R. (1991). A compensated-Redlich-Kwong (CORK) equation for volumes and fugacities of CO2 and H2O in the range 1 bar to 50 kbar and 100?1600C. *Contributions to Mineralogy and Petrology*, *109*(2), 265–273. https://doi.org/10.1007/BF00306484

Holland, T. J. B. (1990). Activities in omphacite solid solutions: An application of Landau theory to mixtures. *Contributions to Mineralogy and Petrology*, *105*, 446–453. https://doi.org/10.1007/BF00286831

Holland, T. J. B., & Powell, R. (1998). An internally consistent thermodynamic data set for phase of petrological interest. *Journal of Metamorphic Geology*, *16*(3), 309–343. https://doi.org/10.1111/j.1525-1314.1998.00140.x

Hoover, W. F., Penniston-Dorland, S., Baumgartner, L., Bouvier, A.-S., Dragovic, B., Locatelli, M., Angiboust, S., & Agard, P. (2022). Episodic fluid flow in an eclogite-facies shear zone: Insights from li isotope zoning in garnet. *Geology*, *50*(6), 746–750. https://doi.org/10.1130/G49737.1

Incel, S., Hilairet, N., Labrousse, L., John, T., Deldicque, D., Ferrand, T., Wang, Y., Renner, J., Morales, L., & Schubnel, A. (2017). Laboratory earthquakes triggered during eclogitization of lawsonite-bearing blueschist. *Earth and Planetary Science Letters*, *459*, 320–331. https://doi.org/10.1016/j.epsl.2016.11.047

Ingrin, J., Doukhan, N., & Doukhan, J. C. (1991). High-temperature deformation of diopside single crystal: 2. Transmission electron microscopy investigation of the defect microstructures. *Journal of Geophysical Research - Solid Earth*, *96*(B9), 14287–14297. https://doi.org/10.1029/91JB01233

Ingrin, J., & Madon, M. (1995). TEM observations of several spinel-garnet assemblies: Toward the rheology of the transition zone. *Terra Nova*, *7*(5), 509–515. https://doi.org/10.1111/j.1365-3121.1995.tb00552.x

Jamtveit, B., Ben-Zion, Y., Renard, F., & Austrheim, H. (2018). Earthquake-induced transformation of the lower crust. *Nature*, *556*(7702), 487–491. https://doi.org/10.1038/s41586-018-0045-y

Jin, Z.-M., Zhang, J., Green, H. W. II, & Jin, S. (2001). Eclogite rheology: Implications for subducted lithosphere. *Geology*, *29*(8), 667. https://doi.org/10.1130/0091-7613(2001)029<0667:ERIFSL>2.0.CO;2

John, T., Medvedev, S., Rüpke, L., Andersen, T. B., Podladchikov, Y. Y., & Austrheim, H. (2009). Generation of intermediate-depth earthquakes by self-localizing thermal runaway. *Nature Geoscience*, *2*, 137–140. https://doi.org/10.1038/ngeo419

John, T., & Schenk, V. (2006). Interrelations between intermediate-depth earthquakes and fluid flow within subducting oceanic plates: Constraints from eclogite facies pseudotachylytes. *Geology*, *34*(7), 557. https://doi.org/10.1130/G22411.1

Jung, H., Green, I. H. W., & Dobrzhinetskaya, L. F. (2004). Intermediate-depth earthquake faulting by dehydration embrittlement with negative volume change. *Nature*, *428*, 545–549. https://doi.org/10.1038/nature02412

Kirby, S. H. (1987). Localized polymorphic phase transformations in high-pressure faults and applications to the physical mechanism of deep earthquakes. *Journal of Geophysical Research - Solid Earth*, *92*(B13), 13789–13800. https://doi.org/10.1029/JB092iB13p13789

Kohn, M. J. (2020). A refined zirconium-in-rutile thermometer. *American Mineralogist*, *105*(6), 963–971. https://doi.org/10.2138/am-2020-7091

Kullerud, K. (1987). Origin and tectonometamorphic evolution of the eclogites in the Tsäkkok Lens (Seve Nappes), Southern Norrbotten, Sweden *(PhD Thesis)*. University of Oslo.

Kullerud, K., Stephens, M. B., & Zachrisson, E. (1990). Pillow lavas as protoliths for eclogites: Evidence from a late Precambrin-Cambrian continental margin, Seve nappes, Scandinavian Caledonides. *Contributions to Mineralogy and Petrology*, *105*, 1–10. https://doi.org/10.1007/BF00320962

Locock, A. J. (2014). An excel spreadsheet to classify chemical analyses of amphiboles following the IMA 2012 recommendations. *Computers & Geosciences*, *62*, 1–11. https://doi.org/10.1016/j.cageo.2013.09.011

Lü, Z., Zhang, L., Du, J., & Bucher, K. (2009). Petrology of coesite-bearing eclogite from Habutengsu Valley, western Tianshan, NW China and its tectonometamorphic implication. *Journal of*

15251314, 0, Downloaded from https://onlinelibrary.wiley.com/doi/10.1111/jmg.12765 by Universidad De Granada, Wiley Online Library on [11/04/2024]. See the Terms and Conditions (https://onlinelibrary.wiley.com/terms-and-conditions) on Wiley Online Library for rules of use; OA articles are governed by the applicable Creative Commons License

*Metamorphic Geology*, *27*(9), 773–787. https://doi.org/10.1111/j.1525-1314.2009.00845.x

Luvizotto, G. L., & Zack, T. (2009). Nb and Zr behavior in rutile during high-grade metamorphism and retrogression: An example from the Ivrea–Verbano Zone. *Chemical Geology*, *261*(3–4),303–317. https://doi.org/10.1016/j.chemgeo.2008.07.023

Mainprice, D., & Nicolas, A. (1989). Development of shape and lattice preferred orientations: Application to the seismic anisotropy of the lower crust. *Journal of Structural Geology*, *11*(1–2), 175–189. https://doi.org/10.1016/0191-8141(89)90042-4

Mauler, A., Godard, G., & Kunze, K. (2001). Crystallographic fabrics of omphacite, rutile and quartz in Vendée eclogites (Armorican massif, France). Consequences for deformation mechanisms and regimes. *Tectonophysics*, *342*(1–2), 81–112. https://doi.org/10.1016/S0040-1951(01)00157-3

Miller, S. A., van der Zee, W., Olgaard, D. L., & Connolly, J. A. D. (2003). A fluid-pressure feedback model of dehydration reactions: Experiments, modelling, and application to subduction zones. *Tectonophysics*, *370*(1–4), 241–251. https://doi.org/10.1016/S0040-1951(03)00189-6

Morimoto, N., Fabries, J., Ferguson, A. K., Ginzburg, I. V., Ross, M., Seifert, F. A., & Zussman, J. (1988). Nomenclature of pyroxenes. *Mineralogical Magazine*, *52*, 535–550. https://doi.org/10.1180/minmag.1988.052.367.15

Mørk, M. B. E., Kullerud, K., & Stabel, A. (1988). Sm-Nd dating of Seve eclogites, Norrbotten, Sweden - evidence for early Caledonian (505 ma) subduction. *Contributions to Mineralogy and Petrology*, *99*(3), 344–351. https://doi.org/10.1007/BF00375366

Newton, R. C., Charlu, T. V., & Kleppa, O. J. (1980). Thermochemistry of the high structural state plagioclases. *Geochimica et Cosmochimica Acta*, *44*(7), 933–941. https://doi.org/10.1016/0016-7037(80)90283-5

Okamoto, K., & Maruyama, S. (1999). The high-pressure synthesis of lawsonite in the MORB+H $_2$ O system. *American Mineralogist*, *84*(3), 362–373. https://doi.org/10.2138/am-1999-0320

Padrón-Navarta, J. A., Lopez Sanchez-Vizcaino, V., Garrido, C. J., & Gomez-Pugnaire, M. T. (2011). Metamorphic record of high-pressure dehydration of antigorite Serpentinite to chlorite Harzburgite in a subduction setting (Cerro del Almirez, Nevado-Filabride complex, southern Spain). *Journal of Petrology*, *52*(10), 2047–2078. https://doi.org/10.1093/petrology/egr039

Palin, R. M., St-Onge, M. R., Waters, D. J., Searle, M. P., & Dyck, B. (2014). Phase equilibria modelling of retrograde amphibole and clinozoisite in mafic eclogite from the Tso Morari massif, Northwest India: Constraining the *P* - *T* - *M* (H $_2$ O) conditions of exhumation. *Journal of Metamorphic Geology*, *32*(7), 675–693. https://doi.org/10.1111/jmg.12085

Peacock, S. M. (2001). Are the lower planes of double seismic zones caused by serpentine dehydration in subducting oceanic mantle? *Geology*, *29*(4), 299. https://doi.org/10.1130/0091-7613(2001)029<0299:ATLPOD>2.0.CO;2

Penniston-Dorland, S. C., Kohn, M. J., & Piccoli, P. M. (2018). A mélange of subduction temperatures: Evidence from Zr-in-rutile thermometry for strengthening of the subduction interface. *Earth and Planetary Science Letters*, *482*, 525–535. https://doi.org/10.1016/j.epsl.2017.11.005

Petley-Ragan, A., Plümper, O., Ildefonse, B., & Jamtveit, B. (2020). Nano-scale earthquake records preserved in plagioclase microfractures from the lower continental crust. *Solid Earth*, *2020*, 1–14.

Philippon, M., Gueydan, F., Pitra, P., & Brun, J.-P. (2013). Preservation of subduction-related prograde deformation in lawsonite pseudomorph-bearing rocks. *Journal of Metamorphic Geology*, *31*(5), 571–583. https://doi.org/10.1111/jmg.12035

Piepenbreier, D., & Stöckhert, B. (2001). Plastic flow of omphacite in eclogites at temperatures below 500°C – Implications for interplate coupling in subduction zones. *International Journal of Earth Sciences*, *90*(1), 197–210. https://doi.org/10.1007/s005310000159

Pognante, U., & Kienast, J.-R. (1987). Blueschist and Eclogite transformations in Fe-Ti Gabbros: A case from the Western Alps ophiolites. *Journal of Petrology*, *28*(2), 271–292. https://doi.org/10.1093/petrology/28.2.271

Poli, S., & Schmidt, M. W. (1995). H2O transport and release in subduction zones: Experimental constraints on basaltic and andesitic systems. *Journal of Geophysical Research - Solid Earth*, *100*(B11), 22299–22314. https://doi.org/10.1029/95JB01570

Powell, R., & Holland, T. (1999). Relating formulations of the thermodynamics of mineral solid solutions; activity modeling of pyroxenes, amphiboles, and micas. *American Mineralogist*, *84*(1–2), 1–14. https://doi.org/10.2138/am-1999-1-201

Putnis, A., Jamtveit, B., & Austrheim, H. (2018). Metamorphic processes and seismicity: The Bergen arcs as natural laboratory. *Journal of Petrology*, *58*(10), 1871–1898. https://doi.org/10.1093/petrology/egx076

Raterron, P., Doukhan, N., Jaoul, O., & Doukhan, J. C. (1994). High temperature deformation of diopside IV: Predominance of {110} glide above 1000°C. *Physics of the Earth and Planetary Interiors*, *82*(3–4), 209–222. https://doi.org/10.1016/0031-9201(94)90073-6

Ravna, E. J., & Terry, M. P. (2004). Geothermobarometry of UHP and HP eclogites and schists - an evaluation of equilibria among garnet-clinopyroxene-kyanite-phengite-coesite/quartz. *Journal of Metamorphic Geology*, *22*(6), 579–592. https://doi.org/10.1111/j.1525-1314.2004.00534.x

Ravna, K. (2000). The garnet-clinopyroxene Fe2+ -mg geothermometer: An updated calibration. *Journal of Metamorphic Geology*, *18*(2), 211–219. https://doi.org/10.1046/j.1525-1314.2000.00247.x

Rehman, H. U., Mainprice, D., Barou, F., Yamamoto, H., Wei, C., Zafar, T., & Khan, T. (2023). Crystallographic preferred orientations and microtexture of the Himalayan eclogites revealing records of syn-deformation peak metamorphic stage and subsequent exhumation. *Journal of Structural Geology*, *167*, 104792. https://doi.org/10.1016/j.jsg.2023.104792

Reinsch, D. (1979). Glaucophanites and eclogites from Val Chiusella, Sesia-Lanzo zone (Italian Alps). *Contributions to Mineralogy and Petrology*, *70*(3), 257–266. https://doi.org/10.1007/BF00375355

Ridley, J., & Dixon, J. E. (1984). Reaction pathways during the progressive deformation of a blueschist metabasite: The role of chemical disequilibrium and restricted range equilibrium. *Journal of Metamorphic Geology*, *2*(2), 115–128. https://doi.org/10.1111/j.1525-1314.1984.tb00291.x

Root, D., & Corfu, F. (2012). U–Pb geochronology of two discrete Ordovician high-pressure metamorphic events in the Seve

15251314, 0, Downloaded from https://onlinelibrary.wiley.com/doi/10.1111/jmg.12765 by Universidad De Granada, Wiley Online Library on [11/04/2024]. See the Terms and Conditions (https://onlinelibrary.wiley.com/terms-and-conditions) on Wiley Online Library for rules of use; OA articles are governed by the applicable Creative Commons License

nappe complex, Scandinavian Caledonides. *Contributions to Mineralogy and Petrology*, *163*, 769–788. https://doi.org/10.1007/s00410-011-0698-0

Rubatto, D., & Angiboust, S. (2015). Oxygen isotope record of oceanic and high-pressure metasomatism: A P–T–time–fluid path for the Monviso eclogites (Italy). *Contributions to Mineralogy and Petrology*, *170*(5–6), 44. https://doi.org/10.1007/s00410-015-1198-4

Scambelluri, M., Fiebig, J., Malaspina, N., Müntener, O., & Pettke, T. (2004). Serpentinite subduction: Implications for fluid processes and trace-element recycling. *International Geology Review*, *46*(7), 595–613. https://doi.org/10.2747/0020-6814.46.7.595

Scambelluri, M., Pennacchioni, G., Gilio, M., Bestmann, M., Plümper, O., & Nestola, F. (2017). Fossil intermediate-depth earthquakes in subducting slabs linked to differential stress release. *Nature Geoscience*, *10*(12), 960–966. https://doi.org/10.1038/s41561-017-0010-7

Schmidt, M. W., & Poli, S. (1998). Experimentally based water budgets for dehydrating slabs and consequences for arc magma generation. *Earth and Planetary Science Letters*, *163*(1–4), 361–379. https://doi.org/10.1016/S0012-821X(98)00142-3

Schubnel, A., Brunet, F., Hilairet, N., Gasc, J., Wang, Y., & Green, H. W. (2013). Deep-focus earthquake analogs recorded at high pressure and temperature in the laboratory. *Science*, *341*(6152), 1377–1380. https://doi.org/10.1126/science.1240206

Stephens, M. B., & van Roermund, H. L. M. (1984). Occurence of glaucophane and crossite in eclogites of the Seve nappes, southern Norrbotten Caledonides, Sweden. *Norsk Geologisk Tidsskrift*, *64*, 155–163.

Stöckhert, B., & Renner, J. (1998). Rheology of crustal rocks at ultrahigh pressure. In B. R. Hacker & J. G. Liu (Eds.), *When continents collide: Geodynamics and geochemistry of ultrahigh-pressure rocks* (pp. 57–95). Dordrecht: Springer. https://doi.org/10.1007/978-94-015-9050-1_3

Stünitz, H., Neufeld, K., Heilbronner, R., Finstad, A. K., Konopásek, J., & Mackenzie, J. R. (2020). Transformation weakening: Diffusion creep in eclogites as a result of interaction of mineral reactions and deformation. *Journal of Structural Geology*, *139*, 104129. https://doi.org/10.1016/j.jsg.2020.104129

Svenningsen, O. M. (2001). Onset of seafloor spreading in the Iapetus Ocean at 608 ma: Precise age of the Sarek dyke swarm, northern Swedish Caledonides. *Precambrian Research*, *110*, 241–254. https://doi.org/10.1016/S0301-9268(01)00189-9

Thielmann, M. (2018). Grain size assisted thermal runaway as a nucleation mechanism for continental mantle earthquakes: Impact of complex rheologies. *Tectonophysics*, *746*, 611–623. https://doi.org/10.1016/j.tecto.2017.08.038

Thielmann, M., Rozel, A., Kaus, B. J. P., & Ricard, Y. (2015). Intermediate-depth earthquake generation and shear zone formation caused by grain size reduction and shear heating. *Geology*, *43*(9), 791–794. https://doi.org/10.1130/G36864.1

Tomkins, H. S., Powell, R., & Ellis, D. J. (2007). The pressure dependence of the zirconium-in-rutile thermometer. *Journal of Metamorphic Geology*, *25*(6), 703–713. https://doi.org/10.1111/j.1525-1314.2007.00724.x

Ujiie, K., Saishu, H., Fagereng, Å., Nishiyama, N., Otsubo, M., Masuyama, H., & Kagi, H. (2018). An explanation of episodic tremor and slow slip constrained by crack-seal veins and viscous shear in subduction Mélange. *Geophysical Research Letters*, *45*(11), 5371–5379. https://doi.org/10.1029/2018GL078374

Ulrich, S., & Mainprice, D. (2005). Does cation ordering in omphacite influence development of lattice-preferred orientation? *Journal of Structural Geology*, *27*(3), 419–431. https://doi.org/10.1016/j.jsg.2004.11.003

Urai, J. L., Means, W. D., & Lister, G. S. (1986). Dynamic recrystallization of minerals. In B. E. Hobbs & G. S. Heard (Eds.), *Mineral and rock deformation: Laboratory studies* (pp. 161–199). American Geophysical Union. https://doi.org/10.1029/GM036

van Panhuys-Sigler, M., & Hartman, P. (1981). Morphologie théorique de certains pyroxènes déduite de la structure cristalline. *Bulletin Mineralogy*, *104*, 95–106. https://doi.org/10.3406/bulmi.1981.7441

van Roermund, H. L. M. (1989). High-pressure ultramafic rocks from the Allochthonous Nappes of the Swedish Caledonides. In *The Caledonide geology of Scandinavia* (pp. 205–219). Springer. https://doi.org/10.1007/978-94-009-2549-6_17

van Roermund, H. L. M., & Boland, J. N. (1981). The dislocation substructures of naturally deformed omphacites. *Tectonophysics*, *78*(1–4), 403–418. https://doi.org/10.1016/0040-1951(81)90022-6

Viete, D. R., Hacker, B. R., Allen, M. B., Seward, G. G. E., Tobin, M. J., Kelley, C. S., Cinque, G., & Duckworth, A. R. (2018). Metamorphic records of multiple seismic cycles during subduction. *Science Advances*, *4*(3), eaaq0234. https://doi.org/10.1126/sciadv.aaq0234

Voegelé, V., Liu, B., Cordier, P., Wang, Z., Takei, H., Pan, P., & Karato, S. (1999). High temperature creep in a 2–3–4 garnet: Ca3Ge2Ge3O12. *Journal of Materials Science*, *34*(19), 4783–4791. https://doi.org/10.1023/A:1004695307022

Wang, Z., & Ji, S. (1999). Deformation of silicate garnets; brittle-ductile transition and its geological implications. *The Canadian Mineralogist*, *37*(2), 525–541.

White, R. W., Powell, R., Holland, T. J. B., & Worley, B. A. (2000). The effect of TiO $_2$ and $Fe_2O_3$ on metapelitic assemblages at greenschist and amphibolite facies conditions: Mineral equilibria calculations in the system $K_2O$-FeO-MgO-$Al_2O_3$-$SiO_2$-$H_2O$-$TiO_2$-$Fe_2O_3$. *Journal of Metamorphic Geology*, *18*(5), 497–511. https://doi.org/10.1046/j.1525-1314.2000.00269.x

White, R. W., Powell, R., & Holland, T. J. B. (2007). Progress relating to calculation of partial melting equilibria for metapelites. *Journal of Metamorphic Geology*, *25*(5), 511–527. https://doi.org/10.1111/j.1525-1314.2007.00711.x

Whitney, D. L., & Evans, B. W. (2010). Abbreviations for names of rock-forming minerals. *American Mineralogist*, *95*, 185–187. https://doi.org/10.2138/am.2010.3371

Wright, S. I., Nowell, M. M., & Field, D. P. (2011). A review of strain analysis using electron backscatter diffraction. *Microscopy and Microanalysis*, *17*(3), 316–329. https://doi.org/10.1017/S1431927611000055

Yamato, P., Duretz, T., & Angiboust, S. (2019). Brittle/ductile deformation of Eclogites: Insights from numerical models. *Geochemistry, Geophysics, Geosystems*, *20*(7), 3116–3133. https://doi.org/10.1029/2019GC008249

Yang, J.-J., Huang, M.-X., Wu, Q.-Y., & Zhang, H.-R. (2014). Coesite-bearing eclogite breccia: Implication for coseismic ultrahigh-pressure metamorphism and the rate of the process.

15251314, 0, Downloaded from https://onlinelibrary.wiley.com/doi/10.1111/jmg.12765 by Universidad De Granada, Wiley Online Library on [11/04/2024]. See the Terms and Conditions (https://onlinelibrary.wiley.com/terms-and-conditions) on Wiley Online Library for rules of use; OA articles are governed by the applicable Creative Commons License

*Contributions to Mineralogy and Petrology*, *167*(6), 1013. https://doi.org/10.1007/s00410-014-1013-7

Zack, T., Moraes, R., & Kronz, A. (2004). Temperature dependence of Zr in rutile: Empirical calibration of a rutile thermometer. *Contributions to Mineralogy and Petrology*, *148*(4), 471–488. https://doi.org/10.1007/s00410-004-0617-8

Zhang, J., Green, H., & Bozhilov, K. (2006). Rheology of omphacite at high temperature and pressure and significance of its lattice preferred orientations. *Earth and Planetary Science Letters*, *246*(3–4), 432–443. https://doi.org/10.1016/j.epsl.2006.04.006

Zhang, J., & Green, H. W. (2007). Experimental investigation of Eclogite rheology and its fabrics at high temperature and pressure. *Journal of Metamorphic Geology*, *25*(2), 97–115. https://doi.org/10.1111/j.1525-1314.2006.00684.x

## SUPPORTING INFORMATION

Additional supporting information can be found online in the Supporting Information section at the end of this article.

**Figure S1.** X-ray maps of omphacite (TS17–58D).
**Figure S2.** X-ray maps of garnet (TS17–58D and TS17–67).
**Figure S3.** Microstructures and intragranular lattice distortion of omphacite.
**Figure S4.** Detailed petrographic features.
**Figure S5.** Results of thermodynamic modelling and EBSD mapping (Ph-free sample TS17–67).
**Figure S6.** Results of thermodynamic modelling and EBSD mapping (Ph-bearing sample KF16–21).
**Table S1.** GPS coordinates of the studied outcrops.
**Table S2.** Bulk rock composition.
**Table S3.** Bulk composition for thermodynamic modelling.
**Table S4.** Representative WDS analyses of garnet, omphacite, amphibole and white mica.
**Table S5.** Representative WDS analyses of rutile and results of Zr-in-Rt thermometry.

**How to cite this article:** Bukała, M., Hidas, K., Klonowska, I., Barnes, C. J., Fassmer, K., & Majka, J. (2024). Dehydration-driven deformation of eclogite: Interplay between fluid discharge and rheology. *Journal of Metamorphic Geology*, 1–28. https://doi.org/10.1111/jmg.12765

15251314, 0, Downloaded from https://onlinelibrary.wiley.com/doi/10.1111/jmg.12765 by Universidad De Granada, Wiley Online Library on [11/04/2024]. See the Terms and Conditions (https://onlinelibrary.wiley.com/terms-and-conditions) on Wiley Online Library for rules of use; OA articles are governed by the applicable Creative Commons License